Flexible Active Power Control of Distributed Photovoltaic Systems with Integrated Battery using Series Converter Configurations

Pan, Yiwei; Sangwongwanich, Ariya; Yang, Yongheng; Liu, Xiong; Liserre, Marco; Blaabjerg, Frede

Published in:
IEEE Journal of Emerging and Selected Topics in Power Electronics

DOI (link to publication from Publisher):
10.1109/JESTPE.2021.3134203

Publication date:
2022

Document Version
Accepted author manuscript, peer reviewed version

Flexible Active Power Control of Distributed Photovoltaic Systems with Integrated Battery using Series Converter Configurations

Yiwei Pan, *Student Member, IEEE*, Ariya Sangwongwanich, *Member, IEEE*, Yongheng Yang, *Senior Member, IEEE*, Xiong Liu, *Senior Member, IEEE*, Marco Liserre, *Fellow, IEEE*, and Frede Blaabjerg, *Fellow, IEEE*

***Abstract*—Flexible active power control (FAPC) is becoming mandatory for PV systems, which is to limit/reserve the PV power below certain constraints as commanded, including the power ramp-rate control (PRRC), power limiting control (PLC), and power reserve control (PRC). In practice, energy storage such as batteries can be adopted to reduce the PV energy discarding in such cases. On the other hand, concerning the system overall cost, single-stage series power converter configurations are becoming attractive. Such configurations bring more flexibilities by integrating PV systems and batteries. However, the implementation of FAPC functions in series power converter configurations has not been systematically investigated. To fill this gap, the PRRC, PLC, and PRC strategies for series-PV-battery systems are developed in this paper. With the proposed strategies, the power ramp-rate/limiting/reserve constraints are maintained by the coordinated control of individual converters. The reserved power is then distributed among all converters depending on the available power of individual PV converters, battery power and state-of-charge (SoC) conditions. Experimental tests performed on a 1.6-kW system have validated the effectiveness of the proposed solution.**

***Index Terms*—Coordinated control, photovoltaic-battery systems, power limiting control, power ramp-rate control, power reserve control, series-connected converters**

I. Introduction

Increasing integration of renewable energy has made structural changes to the modern power distribution system, and certain adverse impacts have also been seen, e.g., voltage and frequency fluctuations and overloading of the distribution grid [1]-[6]. To avoid these issues and enhance the stability of distributed generation (DG) systems, the power generation of DG units should be more dispatchable, i.e., DG units are required to provide flexible power control functions, in addition to the conventional maximum power injection operation, as shown in Fig. 1(a) [1]-[6]. The flexible active power control (FAPC) for photovoltaic (PV) systems, also referred to as flexible power point tracking (FPPT), is to limit the output PV power to a specific value [1]-[3]. Three main FAPC functionalities for PV systems have been introduced in recent grid regulations, as illustrated in Fig. 1, including the power limiting control (PLC), power reserve control (PRC), and power ramp-rate control (PRRC) [1], [2]. Accordingly, several approaches have been developed in the literature to achieve the above functionalities, where integrating the energy storage (ES) such as batteries with DG systems is one common solution [1], [7], [8].

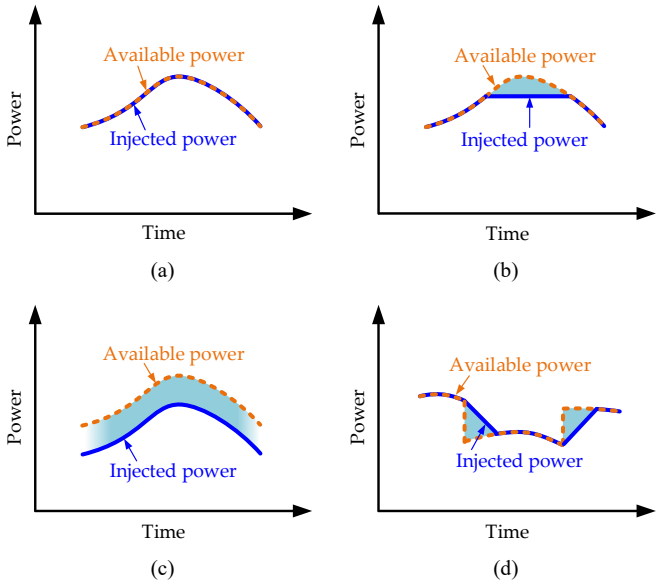

Fig. 1. Flexible power control functionalities of PV systems: (a) conventional maximum power point tracking (MPPT) operation, (b) power limiting control, (c) power reserve control, and (d) power ramp-rate control [1], [2].

To integrate distributed PV panels and batteries, two-stage configurations have been widely used, where low-voltage (LV) PV and battery units are firstly interfaced to DC/DC boost converters to obtain DC voltages suitable for inverting [8]-[11]. Then, the DC rails can be connected to the grid through either separate inverters or a high power inverter, as demonstrated in Figs. 2(a) and (b), respectively. On the other hand, by series-connecting the outputs of multiple DC/DC converters, a DC bus

Manuscript received August 3, 2021; revised October 26, 2021; accepted November 29, 2021. This work was supported in part by the research project – Reliable Power Electronic based Power Systems (REPEPS) by THE VELUX FOUNDATIONS under Award Ref. No.: 00016591, and in part by the National Natural Science Foundation of China (Project no.: 52107212). *(Corresponding Author: Yongheng Yang.)*

Y. Pan, A. Sangwongwanich, and F. Blaabjerg are with the AAU Energy, Aalborg University, Aalborg 9220, Denmark (e-mail: ypa@energy.aau.dk; ars@energy.aau.dk; fbl@energy.aau.dk).

Y. Yang is with the College of Electrical Engineering, Zhejiang University, Hangzhou 310027, China (e-mail: yang_yh@zju.edu.cn).

X. Liu is with the Energy Electricity Research Center, International Energy College, Jinan University, Zhuhai 519070, China (e-mail: liushawn123@ieee.org).

M. Liserre is with the Chair of Power Electronics, Kiel University, Kiel 24143, Germany (e-mail: ml@tf.uni-kiel.de).

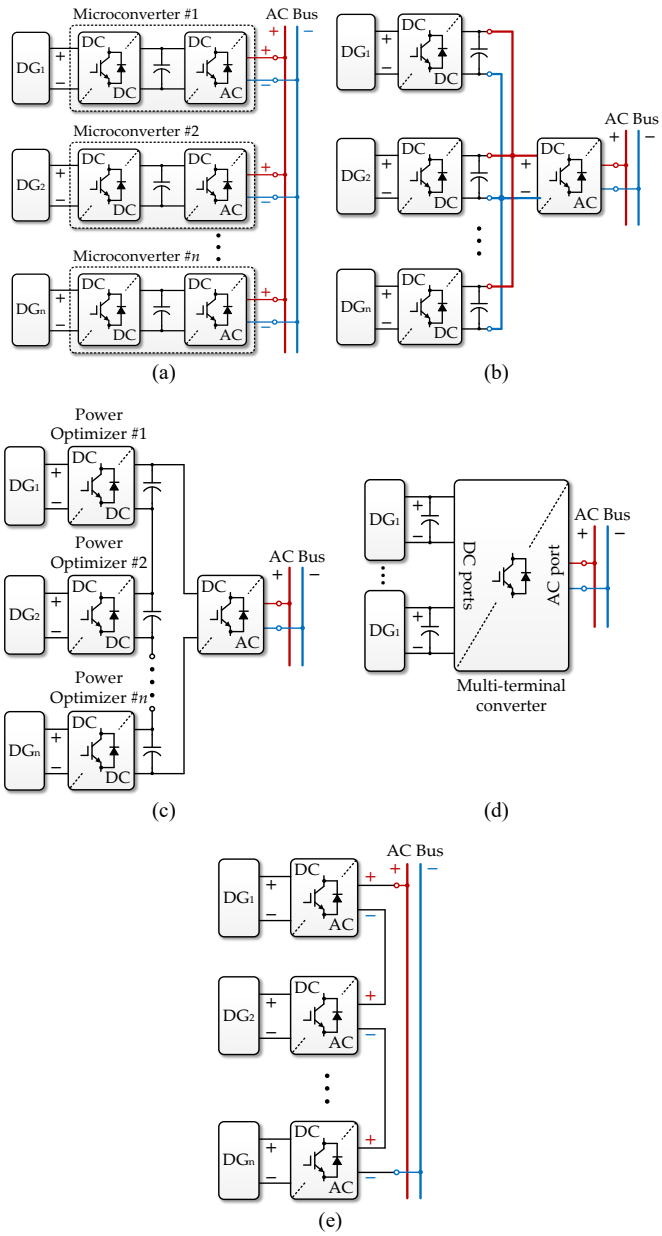

Fig. 2. Configurations of distributed generation systems: (a) parallel connected microconverters, (b) parallel connected DC/DC converters with a common inverter, (c) the power optimized structure, (d) the multi-terminal converter structure, and (e) series-connected LV converters.

with its voltage suitable for grid connection can be obtained with only LV components, as shown in Fig. 2(c). The two configurations in Figs. 2(a) and (c) are both commercially available for distributed PV systems, being known as the microconverter and power optimizer, respectively [1], [11]. Although module-level maximum power point tracking (MPPT) control can be achieved for systems in Figs. 2(a), (b), and (c), the efficiency of the system is compromised due to multiple conversion stages. To simplify the conversion, several advanced topologies have been developed, where PV and battery units can be integrated with multi-terminal converters [12]-[14], as shown in Fig. 2(d). For instance, in [12], the battery is integrated by paralleling with a capacitor in a quasi-Z-source network. In [13], a dual-DC-port asymmetrical multilevel inverter topology is proposed, where LV PV or battery units can be directly interfaced to the LV terminal, eliminating an additional DC/DC boost stage. However, the multi-terminal configurations are more suitable for centrally controlled systems, as the control and modulation for the system are usually complex due to the coupling among multi-terminals. For distributed systems, the implementation of such topologies can be difficult, especially when PV and battery units are geographically far away from each other. In addition, considering the electromagnetic compatibility (EMC) requirements, DG units should be close to the converter in certain multi-port configurations to optimize circulating loops [12], [14]. This further requires more efforts in terms of practical installations.

To integrate distributed PV panels and batteries in a more cost-effective and simpler way, single-stage series configurations have been introduced [8], [15]-[19], as demonstrated in Fig. 2(e). By connecting the AC outputs of distributed inverters in series, LV PV and battery units can be directly interfaced into separate LV DC rails, and thereby being integrated to the AC grid without any additional boost stages [8]. Due to the modular configuration, more PV or battery units can be integrated to the system by simply connecting more series converters. If isolated DC/DC converters are equipped for PV units, the series configuration can be easily connected to grids with a higher voltage (e.g., medium voltage grid), where more LV converter cells are cascaded. While for the configurations in Figs. 2(a)-(d), the system cost will be significantly increased when connecting to high voltage grids, as either components with higher voltage ratings or multilevel topologies with a larger number of components should be employed. Compared with conventional parallel structures shown in Figs. 2(a) and (b), certain limitations remain in series configurations, e.g., higher requirements for hardware redundancy [20], higher common mode voltage and severer leakage current issues [21], limited operation region [22], [23], and higher requirement for synchronization [24], etc. Accordingly, solutions have been developed in [20], [21], [23] and [24] to tackle these issues. Nevertheless, the series configuration remains a cost-effective solution for DG systems.

On the other hand, the distributed power control for series-PV-battery systems is still challenging. Among prior-art control schemes for series-connected systems, most of them are not applicable for series-PV-battery systems, as only ideal or the same type of dc sources (e.g., either only PVs and batteries) with equal power sharing were considered [25]-[28]. Only in a few studies, the control of series-PV-battery systems have been discussed. One typical distributed control approach for series-PV-battery systems is the current-/voltage-mode (CVM) control [17], [18], where one or several converters are centrally controlled as a current source converter, while the others are distributed controlled as voltage source converters [17], [18], [29]-[32]. However, the control methods in [17], [18], [29]-[32] are not applicable for series systems when the power factors (PFs) of individual voltage controlled converters are different,

while real-time communication or additional grid-voltage sensors are still required for current-controlled converters [31]. To overcome this, a distributed control scheme was recently proposed in [33], where distributed PV converters can be self-synchronized without the grid phase angle information, even if they have different PFs, significantly reducing the communication dependency. The anti-over-modulation (AOM) control and the reactive power distribution among all converters have also been addressed in [33]. Nevertheless, the solution in [33] is only for islanded applications, where the overall control objective for the entire series-PV-battery system is to maintain the islanded grid voltage and frequency.

Various FAPC strategies have been developed for PV converters [1], [3]-[5]. However, when directly applying them to series-PV-battery systems, the power control performance may not be satisfying, as explained in the following:

1) Prior-art PRRC, PLC, and PRC methods are only suitable for one single PV inverter. When multiple converters are involved in the system, if the curtailed/reserved power is not properly distributed, PV converters can be unevenly loaded. In extreme cases, the system may be operated beyond its allowed operational region (certain converters over-modulated) [34].
2) In conventional solutions, the excessive power is directly discarded because no batteries were included. However, in series-PV-battery systems, the battery power and state-of-charge (SoC) conditions should be considered when distributing the curtailed/reserved power.
3) To achieve the PRC, the maximum power points (MPPs) of individual PV converters should be periodically observed [5], [35], [36], but different PV converters may operate at their MPPs at the same instant. In such cases, the battery converter cannot absorb all the excessive power to maintain the total power constraints. Especially when a large amount of power reserve is required, the conflicts between the MPP observation and maintaining the power reserve constraint can be much severer.

Several FAPC strategies for series systems have been seen in the literature [17], [37], [38]. For instance, in [17], a decentralized PRRC scheme for series-PV-battery systems has been developed based on the CVM control, where the battery capacity and SoC constraints have not been considered. In other words, when the battery converter fails to provide sufficient power buffering, how to maintain the ramp-rate constraint remains undiscussed. In addition, the FAPC has also been discussed in [37] and [38] where only PV panels are interfaced [37], [38]. In [37], when the grid frequency becomes higher than the upper limit, the PV power will be curtailed based on the droop gain, while the power unbalance among PV converters is not considered. In [38], a cascaded H-bridge (CHB) PV system is controlled as a virtual synchronous generator (VSG), while one PV converter cell with the highest available power is selected for power reserve to provide the power buffer. Nevertheless, the power reserve capability of the entire system is limited, as all required power reserve is assigned to only one PV converter. When the required power reserve increases, the uneven loading among PV converters will be aggravated. Besides, how to compensate the excessive power due to the periodical MPP estimation has not been addressed in [37] and [38]. In other words, when observing the MPP of the system, the total power reserve constraint can no longer be maintained with the strategies in [37] and [38]. In addition, as mentioned previously, more control complexities and constraints (battery power, battery SoC) should be considered when batteries are adopted.

With the above concerns, FAPC strategies are proposed for grid-connected series-PV-battery systems, which is an extension of [39]. The proposed control methods are realized through the distributed control architecture of the series-PV-battery systems [33]. Compared to [33], various active power control schemes (e.g., PRRC, PLC, and PRC) for grid-connected series-PV-battery systems have been developed in this paper. With the proposed strategies, the active power of series-PV-battery systems can be flexibly controlled following the power ramp-rate/limiting/reserve constraints. Considering the battery power capacity, battery SoC condition, the available power of each PV converter and the MPP observation requirements, the surplus PV power can be properly distributed among all converters, which are coordinately controlled to maintain the total power constraints. Notably, compared with [39], the PRC strategy has been additionally developed and evaluated by experiments in this paper, while the operation region of series-PV-battery systems is also analyzed, resulting in stable operation criteria. In addition, more experiments of the PRRC and PLC operation have been performed.

The rest of this paper is organized as follows. In Section II, the distributed control architecture for series-PV-battery systems is introduced. Subsequently, the FAPC strategies for grid-connected series-PV-battery systems are developed in Section III. In Section IV, the stable operation region of the system is investigated and exemplified on a 3-cell system. Experimental tests on a 3-cell 1.6-kW series-PV-battery system are provided to validate the proposed control in Section V. Finally, concluding remarks are given in Section VI.

II. Distributed Control for Series PV-Battery Systems

The configuration and overall control diagram of an n-cell series-PV-battery system is shown in Fig. 3, where n_1 battery converters and n_2 PV converters are connected in series. As observed in Fig. 3, the local controller of one battery converter (the 1st converter in Fig. 3) is responsible for interacting with the upper grid layer control. It sends the operation information of the series-PV-battery system to the grid layer controller for power scheduling, while receives the power constraint commands (power ramp-rate command $P^*_{\text{total,PRR}}$, power limiting command $P^*_{\text{total,lim}}$, and power reserve command $P^*_{\text{total,res}}$) from an upper grid layer, and directly regulates the total active and reactive power accordingly. In certain applications, the constraint commands can also be generated by grid frequency control [2], [38]. Other battery converters, as well as all PV converters are locally controlled through low bandwidth communication (LBC), which is responsible for transmitting

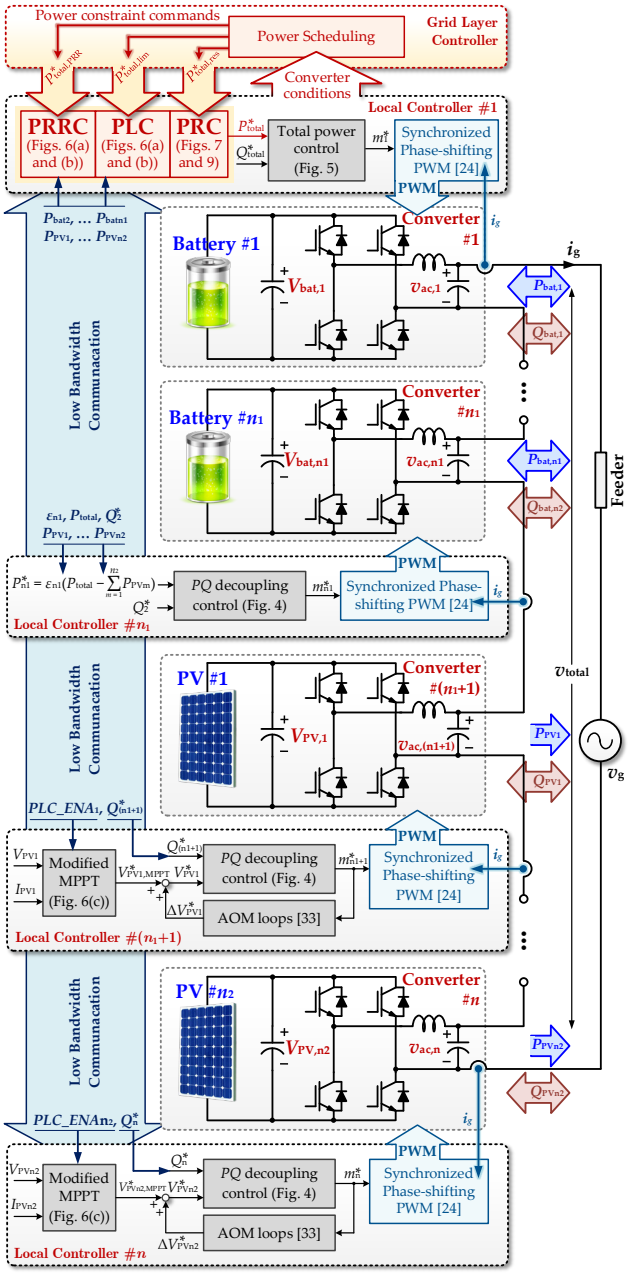

Fig. 3. Power converter scheme of an n-cell series-PVBH system with n_1 battery converters and n_2 PV converters, where $v_{ac,k}$ is the AC voltages of the k^{th} converter, $V_{PV,m}$ and $I_{PV,m}$ are the DC voltage and current of PV #m, respectively, $V_{bat,k}$ is the DC voltage of battery #k, v_{total}, v_g and i_g are the total output AC voltage, grid voltage and grid current of the system, respectively, P^*_{total} and Q^*_{total} are the total active and reactive power reference, respectively, P^*_k, Q^*_k and m^*_k are the active and reactive power reference and the modulation index for the k^{th} converter, respectively, V^*_{PVk} and PLC_ENA_k are the PV voltage reference and power limiting command for PV converter #k, respectively, and $V^*_{PVk,MPPT}$ and ΔV^*_{PVk} are the outputs of the modified MPPT controller and the AOM loop for PV converter #k, respectively.

data for the coordinated control of all converters. To reduce the filter size of individual converters and enhance the quality of the line current i_g, phase-shifting pulse width modulation (PWM) is employed, where the carriers of individual converters are synchronized by the zero-crossing point of the line current, as discussed in [24]. As the output voltages of individual converters are usually nonidentical, variable angle phase shifting PWM methods in [40]-[43] can be employed to further optimize the high-frequency voltage harmonics of the series system.

A. PQ Decoupling Control for PV Converters

The local controllers of all PV converters are the same with those in [33], where a PQ decoupling control is introduced to address the PF-dependent coupling issue between the voltage / frequency (V/f) and the active / reactive power (P/Q) of each converter. The diagram of the PQ decoupling control is shown in Fig. 4, where the active and reactive power of PV converters are regulated by proportional-integral (PI) controllers, with their outputs being decoupled by the decoupling matrix. Then, the increments on the amplitude and angular frequency can be calculated. The active power reference can be obtained by the MPPT control, being either the PV voltage reference $V^*_{PV,m}$ or the PV power reference P^*_k. The output voltage reference of the k^{th} converter $v^*_{ac,k}$ is then calculated by

$$v^*_{ac,k} = V^*_k \sin\left(\int \omega^*_k dt\right) = \left(\frac{V_{g,nom}}{n} + \Delta V_k\right) \sin\left(\int (\omega_{nom} + \Delta\omega_k)\, dt\right). \quad (1)$$

where $V_{g,nom}$ and ω_{nom} are the nominal amplitude and frequency of the grid voltage, respectively, and V^*_k and ω^*_k are the amplitude and frequency references of the ac output voltage for the k^{th} converter, respectively. Then, through the voltage and current dual-loop control, individual power control can be achieved with only local measurements for the PV converters. As the frequency reference ω^*_k is determined locally, the PV converters can be self-synchronized with other converters in the series system without using a phase-locked-loop (PLL) [33]. In addition, the AOM control loops developed in [33] are also included to ensure the stable operation of the system.

B. Control of the Battery Converter

The control diagram of the battery converter is shown in Fig. 5, where the grid current references under the dq-frame (i^*_d and i^*_q) are calculated from the total active and reactive power references (P^*_{total} and Q^*_{total}). Then, the grid current reference i^*_g can be obtained with the grid voltage phase-angle θ_g, which is calculated by a PLL. The grid current is regulated by a proportional-resonant (PR) controller, and the modulation index for the battery converter (m^*_{bat}) can thus be obtained. The total power reference is generated by the FAPC strategies, as illustrated in Fig. 3. With this, the difference between the total power reference and the total power generated by all other converters can be compensated by this battery converter.

For other battery converters, they should also participate in compensating the power difference between the PV power and the constrained total power. Considering the line current can only be directly regulated by one converter in a series system, other battery converters are distributedly controlled with the PQ decoupling control, as shown in Fig. 4. The active power reference P^*_k for the battery converter #k (k = 2, … n_1) is calculated by

$$P^*_k = \varepsilon_k \left(P_{total} - \sum_{m=1}^{n_1} P_{PVm}\right) \quad (2)$$

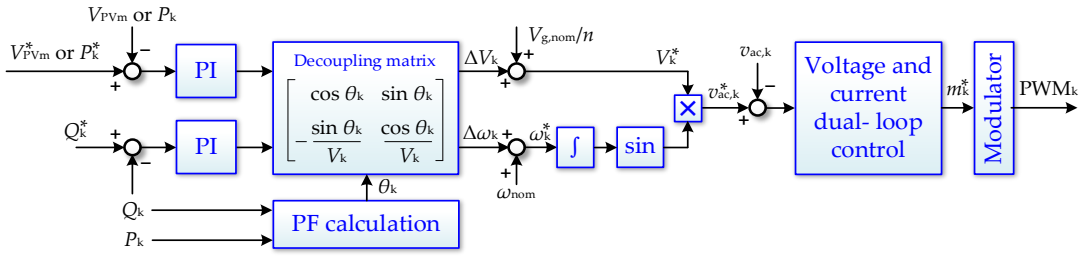

Fig. 4. Power control loops for distributed converters in the series system, where PWM_k refers to the PWM signal for the k^{th} converter [29].

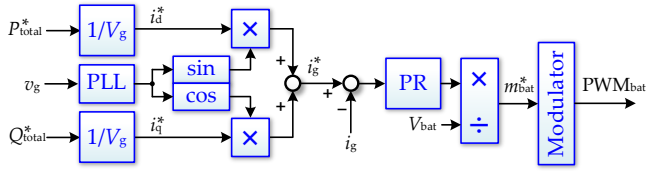

Fig. 5. Power control loops for the battery converter, which is responsible for regulating the total active and reactive power of the entire system (converter #1 in Fig. 3), where m^*_{bat} and PWM_{bat} refer to the modulation index and the PWM signal for this battery converter, respectively.

where ε_k is the power distribution coefficient for the k^{th} battery converter related to the power capacity, SoC, state-of-health (SoH), temperatures, etc [44]. For instance, ε_k can be selected as

$$\varepsilon_k = \mathrm{SoC}_k \cdot C_{bat,k} \Big/ \sum_{m=1}^{n_2} \left(\mathrm{SoC}_m \cdot C_{bat,m}\right) \tag{3}$$

in which $C_{bat,k}$ refers to the capacity of the k^{th} battery. With (2) and (3), the power of each battery converter will be proportional to its remaining capacity, thus ensuring the SoC balancing control among different battery converters.

As the battery power is just proportionally distributed among all battery converters, while the distribution coefficients ε_k have very low dynamics, all battery converters can actually be regarded as one battery unit. Thus, in the following discussion, only one battery converter is considered for simplification (n−1 PV converters for an n-cell system).

III. Flexible Power Control Strategies

In this section, the FAPC strategies for series-PV-battery systems, including the PRRC, PLC, and PRC strategies are developed based on the distributed control architecture introduced in Section II.

A. Power Ramp-Rate and Power Limiting Control

According to the battery power and SoC constraints, there are three operation modes for the proposed PRRC and PLC, as demonstrated in Fig. 6:

1) In normal conditions, all the required active power will be provided by the battery to maintain the PRRC and PLC constraints (Mode 1, Figs. 6(a), (d) and (g)).
2) If the required power is beyond the power limit of the battery converter, the battery will be charged/discharged with its maximum allowed power (Mode 2, Figs. 6(b), (e) and (h)). For the power ramp-up and power limiting control, the remaining part of power is directly curtailed from PV converters, as shown in Figs. 6(b) and (h), respectively. However, for the power ramp-down control, as the battery converter cannot provide sufficient power, the power ramp-rate constraint cannot always be maintained during the power ramp-down, as shown in Fig. 6(e).
3) If the battery SoC reaches its upper or lower limit (SoC_{up} or SoC_{lw}, respectively), no power will be provided by the battery (Mode 3, Figs. 6(c), (f) and (i)). In this mode, all the surplus active power will be discarded from PV converters when the battery SoC > SoC_{up} for the power ramp-up and power limiting control, as shown in Figs. 6(c) and (i), respectively. In such cases, the curtailed power is distributed among PV converters to balance their loading. As it can be noticed from Figs. 6(c) and (i), P_{PV1} and P_{PV2} are curtailed to the same level during the power ramp-up and power-limiting period. On the other hand, the power ramp-rate constraints can no longer be maintained when the battery SoC < SoC_{lw} for the power ramp-down control. Nevertheless, operation conditions in Figs. 6(e) and (f) should be avoided in practice, which can be achieved by increasing the ES capacity of the battery converter.

The corresponding control diagram of the proposed PRRC and PLC strategies is shown in Fig. 7, where the power ramp-rate constraint is maintained through a hysteresis controller. The basic idea of the proposed PRRC for series-PV-battery systems is explained as follows: if the battery power P_{bat} is smaller or larger than its reference P^*_{bat}, the total power reference P^*_{total} will be increased or decreased by P_{step} during each control period, respectively, where $P_{step} = P^*_{total,PRR} T_s$ (T_s refers to the control period). By doing so, the total power reference will be compensated by the battery following the desired ramp-rate $P^*_{total,PRR}$, and in steady state, both the total power and the battery power will oscillate around their power references. Here, the battery power reference P^*_{bat} can be set as zero by default (neither charged nor discharged), or according to the power command from the battery management system (BMS) $P^*_{bat,BMS}$. When $P^*_{bat} = 0$, the battery converter only provides transient power support. To improve the steady-state performance, a small threshold P_{th} is introduced in Fig. 7(a), which can be assigned by two values, with the larger and smaller thresholds being $P_{th,wide}$ and $P_{th,nrrw}$, respectively. When the control enters into the steady-state, i.e., $P^*_{bat} - P_{th} < P_{bat} < P^*_{bat} + P_{th}$, the power threshold P_{th} is set to be larger as $P_{th,wide}$ to avoid frequent variation on P^*_{total}, which usually occur due to MPPT. When the battery power is beyond the range of

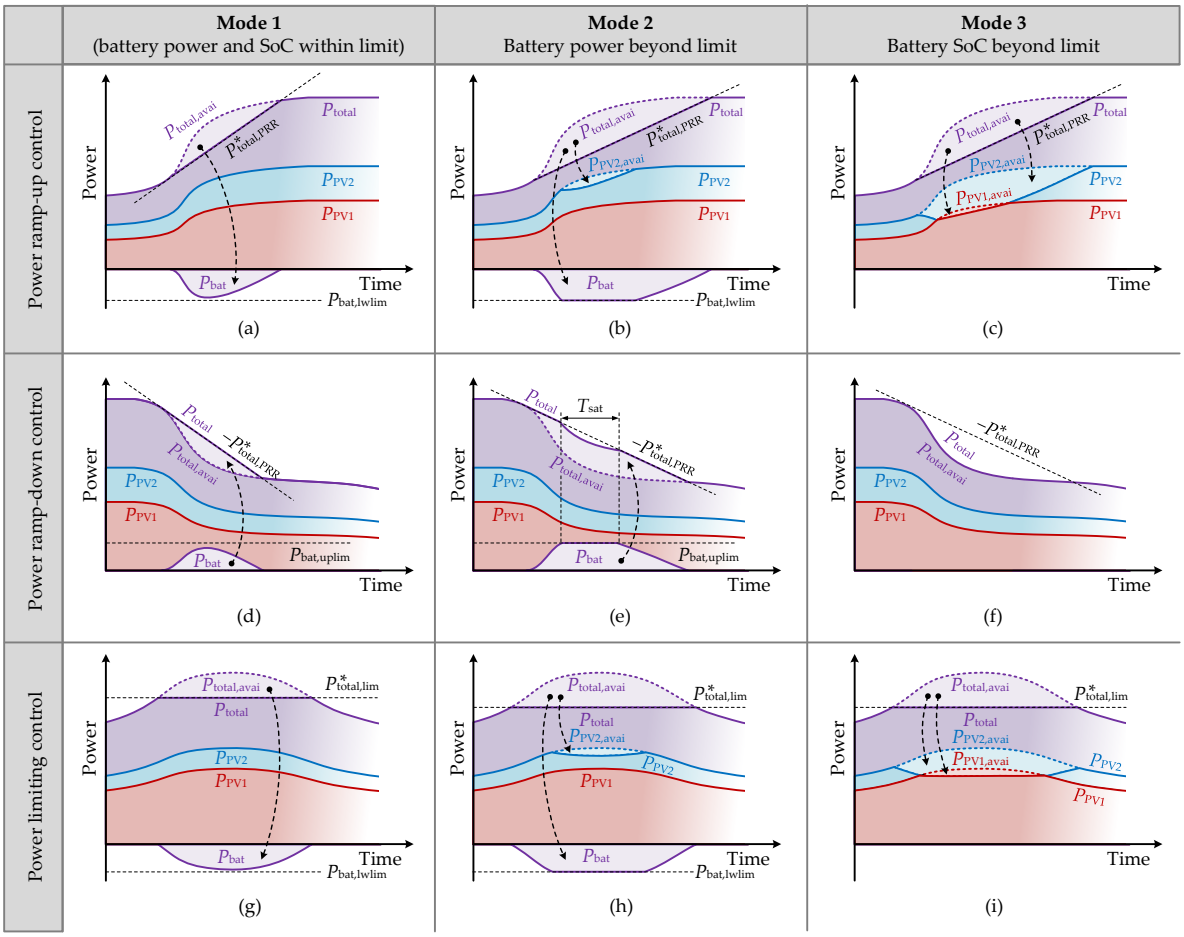

Fig. 6. Three operation modes of a 3-cell series PVBH system with two PV converters under the proposed: (a)-(c) power ramp-up strategy, (d)-(f) power ramp-down strategy, and (c) the power limiting strategy ($P_{\text{total,avai}}$ – total available power; $P_{\text{PV1,avai}}$ and $P_{\text{PV2,avai}}$ – the available power of PV #1 and #2, respectively; $P_{\text{bat,uplim}}$ and $P_{\text{bat,lwlim}}$ – the upper and lower power limit of the battery converter, respectively; and T_{sat} – the period that the power ramp-rate constraint cannot be maintained due to the battery power limitation).

$\left(P^*_{\text{bat}}-P_{\text{th}}, P^*_{\text{bat}}+P_{\text{th}}\right)$, which means the control is in the dynamic zone, $P_{\text{th,nrrw}}$ is assigned to P_{th}, in order to alleviate the steady-state battery power control errors induced by P_{th}. Since P_{th} is very small, it is acceptable in practice, as it has negligible influence on the variation of the battery SoC.

From the above, it is known that the steady-state power of the battery is determined by P^*_{bat}. Thus, the basic idea of the PLC is to set P^*_{bat} as the total surplus active power. As shown in Fig. 7(a), if the PV converters are generating excessive power, the total available power $P^*_{\text{total,avai}}$ will gradually ramp up, and become higher than the power limit $P^*_{\text{total,lim}}$. Subsequently, P^*_{total} will be limited to $P^*_{\text{total,lim}}$ while P^*_{bat} will be set as $\left(P^*_{\text{total,lim}}-P^*_{\text{total,avai}}\right)$, meaning that all the surplus active power will be absorbed by the battery, if the battery power and SoC is within the normal range.

When the battery cannot absorb all excessive PV power (Figs. 6(b) and (h)), a part of PV power will be directly discarded. As shown in Fig. 7(a), P^*_{bat} is limited within the range of [$P_{\text{bat,lwlim}}$, $P_{\text{bat,uplim}}$]. At the same time, the power limiting control of PV converters will be enabled, as shown in Fig. 7(b), where certain PV converters are selected for power curtailment. More specifically, if the power of the i^{th} PV converter is larger than ($P_{\text{PV,max}} - P_{\text{PV,th}}$), this converter will be selected to discard part of its power. Here, $P_{\text{PV,max}}$ is the maximum power among all PV converters, and $P_{\text{PV,th}}$ is a threshold which enables the selection of multiple PV converters for power curtailment. Once the i^{th} converter is chosen, the power-limiting signal for this converter, denoted as PLC_ENA_{i}, will be enabled. When the PLC_ENA signal is received by the i^{th} PV converter through the LBC, the PV voltage reference for the i^{th} PV converter will be increased by $v_{\text{step,PLC}}$ in the next MPPT cycle, instead of being calculated by the conventional MPPT algorithm, as shown in Fig. 7(c). In this way, the battery power only absorbs a part of power with its maximum capability, while the power ramp-rate constraint will be simultaneously maintained by the power limiting control of PV converters, with the power of the selected PV converters curtailed to the same level. In extreme cases when the battery SoC reaches its upper limit (Figs. 6(c) and (i)), $P_{\text{bat,lwlim}}$ will be set as zero to avoid overcharging the battery, as shown in Fig. 7(b). Due to the low bandwidth of the PLC for PV converters, $P_{\text{bat,lwlim}}$ is assigned as a positive value slightly larger than zero ($P_{\text{th,nrrw}}$) to start the PLC for PV converters earlier.

As discussed previously, when the battery converter reaches its upper power limit or SoC limit, the ramp-rate constraint

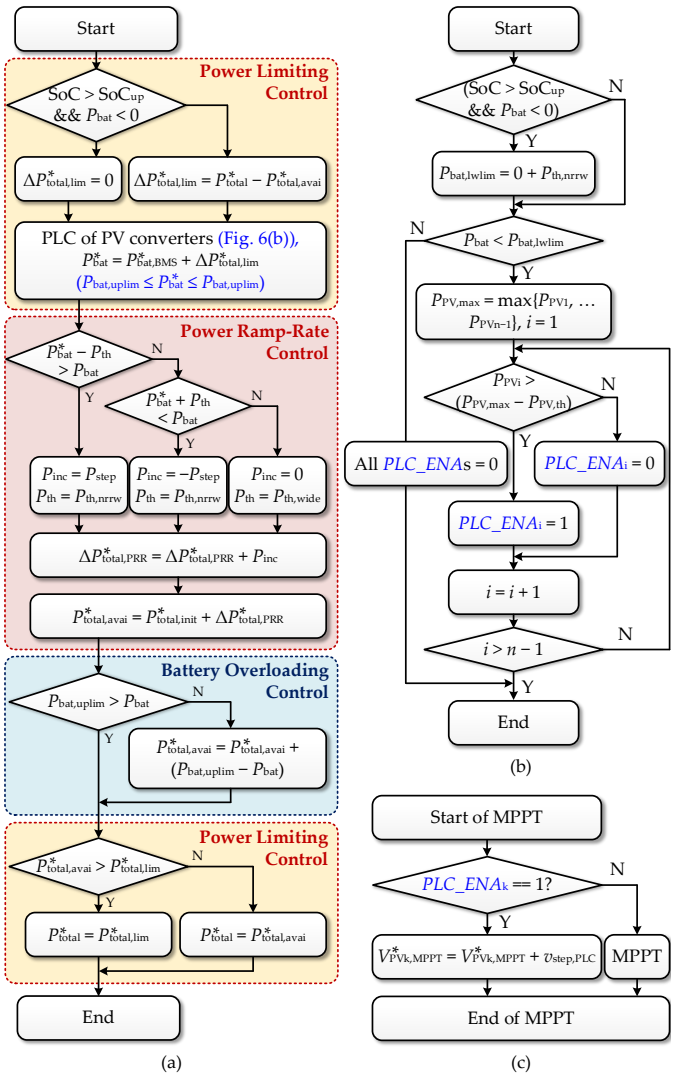

Fig. 7. Diagram of the PRRC and PLC strategy: (a) and (b) the control algorithm implemented in the controller of the battery converter), and (c) modified MPPT algorithm for PV converters ($P^*_{\text{total,init}}$ – initial total power reference; $P^*_{\text{total,avai}}$ – the reference of the total available power; and $\Delta P^*_{\text{total,PRR}}$ – sum of the adjustment (P_{inc}) from the PRRC control).

during the total power ramp-down cannot always be maintained, as shown in Figs. 6(e) and (f). Thus, to avoid overloading the battery in such cases, a battery overloading control is introduced in the proposed PRRC and PLC strategies. As shown in Fig. 7(a), if P_{bat} is higher than $P_{\text{bat,uplim}}$, the excessive power ($P_{\text{bat,uplim}} - P_{\text{bat}}$) will be directly fed forward to the total power reference. In practice, such conditions should be avoided by allocating batteries with sufficient power capacity when designing the series-PV-battery system. As this paper is focused on the FAPC, how to design the capacity of the battery ES system is not detailed.

B. Power Reserve Control

As discussed previously, how to estimate the available PV power during the operation is of importance for the PRC [5]. A cost-effective solution is to employ the sensorless PRC strategy in [5]. The principle of this control is to routinely change the operation of PV inverters between the MPPT mode and the PLC mode. In the MPPT mode, the available PV power is estimated, while the excessive power is temporarily stored in the energy storage elements. When the power at the MPP is determined, the converter operates in the PLC mode to achieve the required power reserve. Inspired by this, in the proposed PRC for series-PV-battery systems, the available PV power is estimated using a similar approach, i.e., through the periodic MPPT control. However, if the MPP observation of individual PV converters is enabled simultaneously, the excessive power will be significantly increased, which can be beyond the power limit of the battery and impossible to be compensated, as demonstrated in Fig. 8(a). In such cases, the total power reserve constraint can no longer be maintained. Thus, in the proposed PRC, the MPPT operations of individual PV converters in the series-PV-battery system are enabled in sequence at different time intervals to achieve module-level MPP estimation for all PV converters, as shown in Figs. 8(b)-(d) and 9. Depending on the MPPT enabling signals (denoted as MPO_ENA_{k} for the k^{th} PV converter), the operation of the k^{th} PV converter can be divided into three periods, as shown in Fig. 9. For the k^{th} converter, Period I refers to the period when the MPPT control is enabled; Period II refers to the period when the MPPT control for all converters is disabled; and Period III refers to the period when the MPPT control is enabled for any other converters. From the above, it is known that the MPPT control is only enabled for at most one converter at any time.

With the MPPT enabling signals, the PRC for series-PV-battery systems has three operating modes depending on battery power and SoC conditions. More specifically, the total reserved power is 1) fully absorbed by the battery, 2) partially curtailed and 3) fully curtailed from PV converters in Modes 1, 2, and 3, respectively, as shown in Figs. 8(b)-(d), where the operating waveforms of a 3-cell PV-battery system with two PV converters are exemplified. In addition, for Modes 2 and 3, the curtailed PV power is distributed among all PV converters to balance their loading.

However, different from the PRRC and PLC strategies, the MPP observation in the PRC can result in an increased excessive power, which may beyond the compensation capability of the battery converter. For such cases, the excessive power can be compensated by the coordinated operation of other PV converters. More clearly, when one PV converter is in the MPPT mode, the power of the other PV converter is further curtailed to maintain the total power reserve constraint, as shown in Figs. 8(c) and (d). Seen from Fig. 10 (zoomed-in plot of Zone 1 in Fig. 8(d)), this further curtailment of PV power appears in Periods III of each PV converter, where all PV converters should be coordinately controlled to maintain the total power reserve constraint. With such an approach, the battery conditions can also be sustained within the normal operation range.

The control flowchart of the PRC is shown in Fig. 11, where the control strategies during Periods I, II, and III for the k^{th} PV converter are developed. The control strategy of PV converters is the same with Fig. 7(c), where PV converters are only dependent on the PLC signals through the LBC to switch their

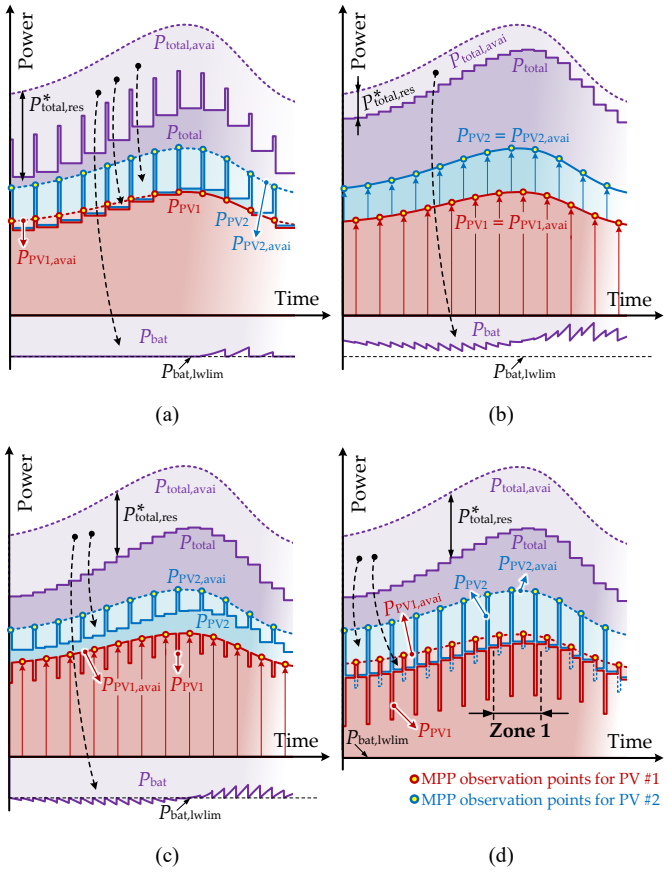

Fig. 8. Operational principle of the PRC: (a) conventional PRC for single inverters are directly applied, (b) Mode 1 of the proposed PRC (battery power and SoC within the normal range), (c) Mode 2 of the proposed PRC (battery power reaches $P_{\text{bat,lwlim}}$), and (d) Mode 3 of the proposed PRC (battery SoC > SoC_{up}), where $P_{\text{PVk,avai}}$ is the available power for the k^{th} PV converter.

operational modes. As shown in Fig. 11, in Period I of the k^{th} PV converter, the MPPT operation of this converter is enabled by setting PLC_ENA_{k} as zero. Then, the available power for the k^{th} PV converter $P_{\text{PVk,avai}}$ will be continuously updated by the historical maximum value of the average active power for the k^{th} PV converter ($P_{\text{PVk,avg}}$), which is obtained from a low pass filter (LPF). Notably, the initial value of $P_{\text{PVk,avai}}$ should be cleared as zero at the beginning of Period I for the following updating. In addition, the PV voltage reference $V^*_{\text{PV,k}}$ can be set as a fraction of its open-circuit voltage $V_{\text{PV,k,OC}}$ at the beginning of Period I, with the fraction F_{v} being in the range of 71−78%, to accelerate the speed of the MPPT [5].

Then, at the beginning of Period II, the power reference of the total available power, denoted as $P^*_{\text{total,avai}}$, will be calculated by summing up all the updated power $P_{\text{PVk,avai}}$ in Period I. Next, a power-limiting threshold $P^*_{\text{PV,PLC}}$ is calculated to limit the power of all PV converters to the same level. Depending on the required total power reserve and the power of the battery converter, there are three cases to calculate this power-limiting threshold $P^*_{\text{PV,PLC}}$, as shown in Fig. 12, where a 4-cell series-PV-battery system with three PV converters is exemplified:

1) Case 1: This case corresponds with Mode 1 shown in Fig. 8(b), where all reserved power is absorbed by the battery converter. In this case, $P^*_{\text{PV,PLC}}$ equals to a large value (larger than the maximum available power among all PV converters), and no power will be curtailed from any PV converters.
2) Case 2: This case corresponds with Modes 2 and 3 shown in Figs. 8(c) and (d), where the power being $P^*_{\text{total,res}} + P_{\text{bat,lwlim}}$ is discarded from PV converters. In this case, not all PV converters are required for power curtailment, as shown in Fig. 12(b), where only the power of two PV converters (PV #1 and #3) is curtailed to $P^*_{\text{PV,PLC}}$. In this case, $P^*_{\text{PV,PLC}}$ is larger than the available power of at least one PV converter.
3) Case 3: In this case, all PV converters are selected for power curtailment, as shown in Fig. 12(c).

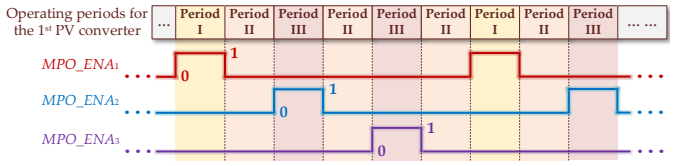

Fig. 9. MPPT enabling signals for series-PV-battery systems.

According to the above, an algorithm is designed to calculate $P^*_{\text{PV,PLC}}$. First, the available power for all PV converters is sorted in a descending order. Then, a new index is assigned to each PV converter, which indicates its power ranking among all PV converters, and is recorded in an array x. In other words, after the sorting, the $x(1)^{\text{th}}$ and $x(n-1)^{\text{th}}$ PV converters will be the PV converters with the maximum and minimum available power, with their available power being denoted as $P_{\text{PVx(1),avai}}$ and $P_{\text{PVx(n−1),avai}}$, respectively. Afterwards, the power limiting threshold $P^*_{\text{PV,PLC}}$ for the above three cases can be obtained, as detailed in the following:

1) Case 1: If $P^*_{\text{total,res}}$ is smaller than $|P_{\text{bat,lwlim}}|$, $P^*_{\text{PV,PLC}}$ will be set as a large value M ($M > P_{\text{PVx(1),avai}}$).
2) Case 2: If $P^*_{\text{total,res}}$ is greater than $|P_{\text{bat,lwlim}}|$, the algorithm will search from the $x(1)^{\text{th}}$ PV converter to the $x(n-1)^{\text{th}}$ PV converter, to determine how many PV converters should be selected for power curtailment. The searching loop is explained as: In the α^{th} cycle of the searching loop, $P^*_{\text{PV,PLC}}$ is assumed to be equal to the available power of the $x(\alpha+1)^{\text{th}}$ PV converter. With this assumption, the total reserved power can be calculated by

$$\Delta P_{\text{comp}} = \sum_{m=1}^{\alpha}\left(P_{\text{PVx(m),avai}} - P_{\text{PVx}(\alpha+1),\text{avai}}\right) \tag{4}$$

where ΔP_{comp} is the assumed power to be curtailed from PV converters, and $P_{\text{PVx(m),avai}}$ refers to all PV converters with their power larger than $P_{\text{PVx}(\alpha+1),\text{avai}}$. If $\Delta P_{\text{comp}} < P^*_{\text{total,res}} - \left|P_{\text{bat,lwlim}}\right|$, α will be increased by 1, and the searching loop will enter the next cycle. Otherwise, the searching loop will be terminated, and the power from the $x(1)^{\text{th}}$ to the $x(\alpha)^{\text{th}}$ PV converters will be curtailed. The power-limiting threshold can be calculated by

$$P^*_{\text{PV,PLC}} = \left(\sum_{m=1}^{\alpha} P^*_{\text{PVx(m),avai}} - P^*_{\text{total,res}} - P_{\text{bat,lwlim}}\right)\Big/\alpha \tag{5}$$

3) Case 3: If $\Delta P^*_{\text{total}}$ is greater than $|P_{\text{bat,lwlim}}|$, and α has reached $n-1$ in the searching loop, all PV converters should be

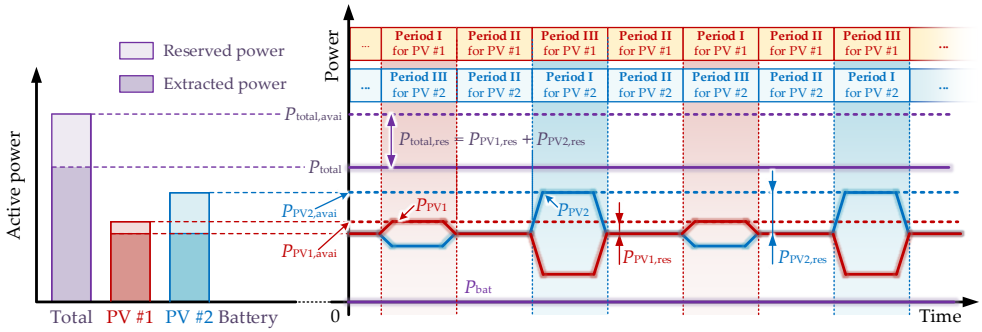

Fig. 10. Variations of the total power and the power from individual converters (zoomed-in plot of Zone 1 in Fig. 8(d)), where $P_{PVk,res}$ is the reserved power of the k^{th} PV converter.

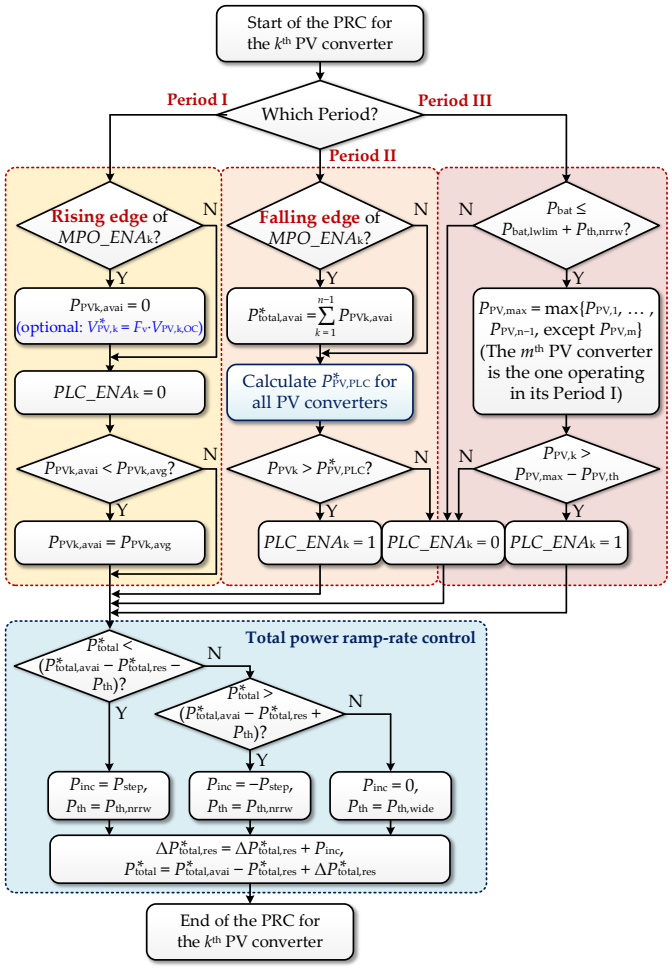

Fig. 11. Control flowcharts of the proposed PRC for series-PV-battery systems.

selected for power curtailment. The power limiting threshold can be calculated by

$$P^*_{PV,PLC} = \left(P^*_{total,avai} - P^*_{total,res} - P_{bat,lwlim}\right) \Big/ (n-1). \quad (6)$$

With the above algorithm, the power limiting reference $P^*_{PV,PLC}$ can be obtained. The power limiting enabling signal for each PV converter can thereby be determined by comparing its power with $P^*_{PV,PLC}$.

In Period III of the k^{th} PV converter, its power may be further curtailed if the battery power or SoC has reached its limits, as illustrated in Figs. 8(c), (d) and 10. Accordingly, when P_{bat} exceeds the lower limit $P_{bat,lwlim}$, the power of the k^{th} PV converter will be curtailed if it is around $P_{PV,max}$, as shown in the control strategy of Period III in Fig. 11. Here, different from the previous definition, $P_{PV,max}$ refers to the maximum power among all PV converters except for the one operating in Period I. In addition, two thresholds are introduced in the control strategy of Period III to avoid frequent disturbances in steady state, being $P_{th,nrrw}$ and $P_{PV,th}$, as shown in Fig. 11.

With the above strategy, the reference of the total available power $P^*_{total,avai}$, and the PLC enabling signals for PV converters can be obtained. Then, P^*_{total} can be calculated by subtracting $P^*_{total,res}$ from $P^*_{total,avai}$. In the proposed control, the variation of P^*_{total} is also regulated following a ramp-rate, which can be achieved by using the hysteresis-control-based PRRC strategy, as shown in Fig. 11. Overall, with the above strategies, module-level MPP estimation and PLC can be achieved for PV converters, while the reserved power is distributed among all converters depending on the power of individual PV converters, battery power and SoC conditions.

C. Parameter Design Consideration of the MPP estimation

The speed to estimate the available power of each converter is dependent on various factors, including the MPPT parameters, the amount of the power reserve, and environmental conditions, etc. According to Fig. 9, the frequency to estimate the total available power $P^*_{total,avai}$ can be described as

$$f_{MPO} = 1/T_{MPO} = 1/\left[T_{P1} + n_2 T_{P2} + (n_2 - 1) T_{P3}\right] \quad (7)$$

where n_2 is the total number of PV converters, T_{MPO} is the period of the MPP estimation signal MPO_ENA_k, and T_{P1}, T_{P2}, and T_{P3} are the duration time of Periods I, II, and III, respectively. In general, $T_{P1} = T_{P3}$, and $f_{MPO} = 1 / (n_2 T_{P1} + n_2 T_{P2})$. Thus, if the minimum T_{P1} and T_{P2} can be found, the maximum f_{MPO} will be determined. Fig. 13 demonstrates the operation waveforms of PV #1 during T_{P1} and T_{P2}, where it can be noticed that both T_{P1} and T_{P2} are determined by 1) the dynamics of the MPPT and 2) the amount of the power reserve. More specifically, T_{P1} and T_{P2} will become longer with a slower MPPT rate. Also, when a larger power reserve is required, it will take more MPPT cycles for PV converters to reach their MPPs or the curtailed value $P^*_{PV,PLC}$. Therefore, considering the worst case where the PV voltage varies between its open-circuit voltage $V_{PV,OC}$

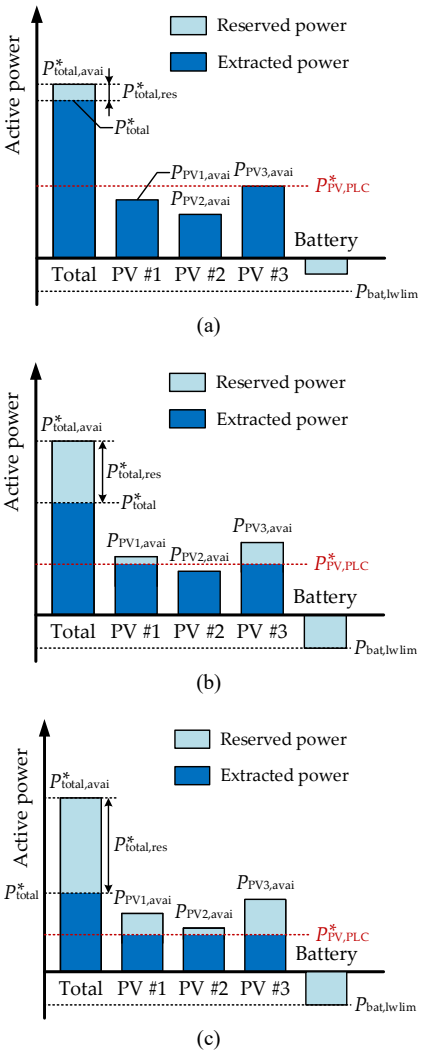

Fig. 12. Three cases to calculate the power limiting threshold of individual PV converters ($P^*_{\mathrm{PV,PLC}}$) for a 4-cell series-PV-battery system with three PV converters: (a) Case 1: no power curtailed from PV converters, (b) Case 2: the power is curtailed from a part of PV converters, and (c) Case 3: the power is curtailed from all PV converters.

($P^*_{\mathrm{PV,PLC}} = 0$) and its MPP voltage V_{MPP} in the PRC, the minimum time for the PV converters to enter the steady states of Periods I and II can be simply estimated as

$$T_{\mathrm{P1,min}} = T_{\mathrm{P2,min}} = N_{\mathrm{MPPT,min}} T_{\mathrm{MPPT}} = T_{\mathrm{MPPT}} \left(V_{\mathrm{PV,OC}} - V_{\mathrm{MPP}} \right) / v_{\mathrm{step}} \quad (8)$$

where $N_{\mathrm{MPPT,min}}$ is the minimum required MPPT cycles. In addition, since LPFs have been employed to calculate the average PV power $P_{\mathrm{PVk,avg}}$, $T_{\mathrm{P1,min}}$ can be longer to ensure a reliable value of $P_{\mathrm{PVk,avg}}$, e.g., T_{P1} can be $(1/f_{\mathrm{LPF,-3dB}})$ longer, where $f_{\mathrm{LPF,-3dB}}$ is the -3 dB bandwidth of the LPF. Since the PV voltage reference can be directly set as $F_{\mathrm{v}} V_{\mathrm{PV,OC}}$ at the beginning of Period I to shorten the required time for MPP estimation, $T_{\mathrm{P1,min}}$ can be equal to $(1/f_{\mathrm{LPF,-3dB}})$, further reducing the required T_{MPO}.

On the other hand, if T_{P1} becomes longer, the estimated maximum available power can be more reliable. If T_{P2} becomes longer, the distribution of the total reserved power among all converters will have better performance, as the power reserve

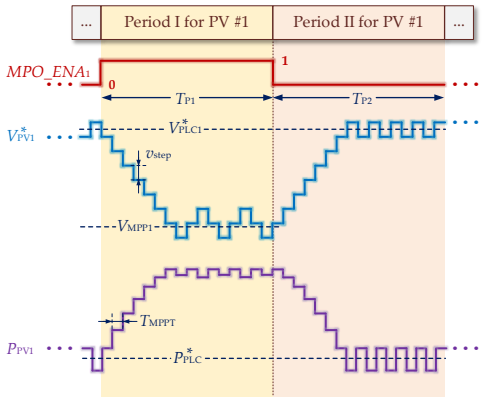

Fig. 13. PV voltage and power for PV converter #1 during Periods I and II of the PRC control, where V_{MPP1} is the MPP voltage of PV #1, v_{step} and T_{MPPT} are the perturbation step-size and the MPPT period, respectively, and V^*_{PLC1} is the PV voltage when the power of PV #1 equals to $P^*_{\mathrm{PV,PLC}}$.

control will be less affected by the MPP estimation. Considering the above, sufficient margins should be involved when determining T_{P1} and T_{P2}. Nevertheless, the MPP estimation does not have to be executed frequently. For instance, in [38], it is executed every 10 minutes. Since the PV power is slowly varying, it is acceptable to select a slow MPP estimation rate in practice.

Notably, even if the PV power changes quickly, the required power reserve can still be maintained with the proposed PRC. For instance, if the PV power increases abruptly after Period I, the power-limiting threshold $P^*_{\mathrm{PV,PLC}}$ will remain unchanged. In the next Period I, the new MPP will be correctly estimated. If the PV power decreases abruptly, e.g., lower than the determined $P^*_{\mathrm{PV,PLC}}$, the PV converter can still be stably operated, i.e., tracking its new MPP lower than $P^*_{\mathrm{PV,PLC}}$ according to the flowchart in Fig. 11. Since $P^*_{\mathrm{total,avai}}$ does not change, the transient power will be provided by the battery. Therefore, longer T_{MPO} just slows down the available power estimation, while the power reserve control can still be achieved.

D. Control-Related Communication Variables

To implement the proposed FAPC strategies, several variables should be transmitted among all converters using the LBC, which include the PV power information (P_{PV1} … $P_{\mathrm{PVn-1}}$), and the PLC enabling signals (PLC_ENA_1 … $PLC\_ENA_{\mathrm{n-1}}$). Since the PLC enabling signals are bit-type variables, they can be combined as one variable for transmission. Compared with the distributed control in [33] for islanded series-PV-battery systems, the only added data for transmission are those PLC enabling signals, which has negligible impact on the communication burden. Therefore, the proposed FAPC strategies can be implemented with very low communication requirements.

IV. Operation Boundary Analysis

As it has been discussed previously, the operation region of series systems is limited due to the risk of over-modulation of individual converters [23], which can be explained with Fig. 14. According to Fig. 14, for a certain grid current, the maximum available power for the battery converter only equals to

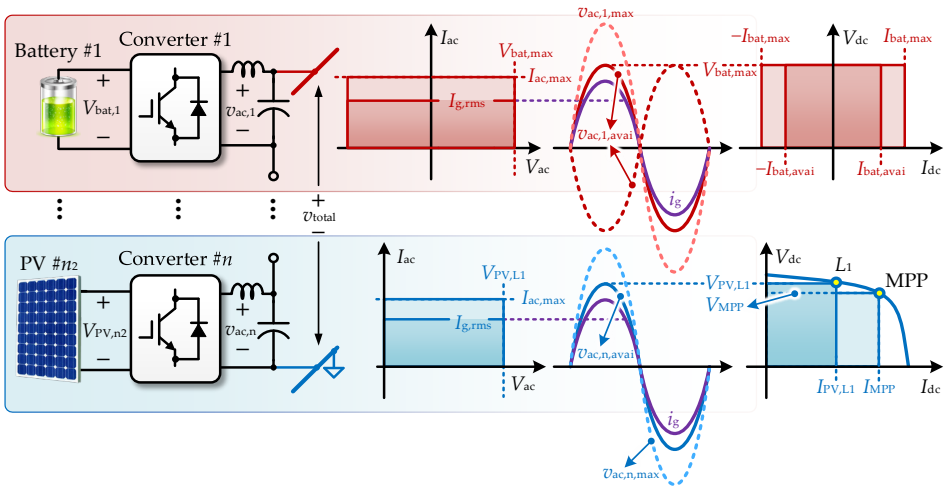

Fig. 14. Demonstration of the limited operation region for individual converters in series-PV-battery systems, where $I_{g,rms}$ is the root mean square (RMS) value of i_g, $V_{bat,max}$ and $I_{bat,max}$ are the maximum voltage and current of the battery, respectively, V_{MPP}, I_{MPP}, $V_{PV,L1}$ and $I_{PV,L1}$ are the PV voltage and current at its MPP and L_1, respectively, $v_{ac,1,avai}$ and $v_{ac,n,avai}$ are the available AC voltages for converter #1 and #n, respectively, and $v_{ac,1,max}$ and $v_{ac,n,max}$ are the assumed AC voltages if converter #1 and #n are generating their maximum power, respectively.

$V_{bat,max}I_g$ / 2, which is lower than its rated power. However, to operate the battery under the rated power, an AC voltage with its amplitude being $v_{ac,1,max}$ should be generated, which is beyond the available DC voltage of the battery converter. Similarly, for the PV converter, its power is limited to $V_{PV,L1}I_g$ / 2, because it will inevitably suffer from over-modulation if it generates its maximum power ($V_{MPP}I_{MPP}$). Thus, for a certain grid current, the available power of both the PV and battery converters are limited by their available DC voltages. Considering that the grid current is determined by all converters and the grid layer constraints, the operation region of each converter is dependent on the operation conditions of other converters. As the converters in a series-PV-battery system are coordinately controlled with the proposed strategies, it is essential to identify the operation limits of the system, which can be helpful for the grid layer control to determine appropriate flexible power commands.

Considering that individual converters should not be over-modulated, the AC voltage amplitude of each converter should not be higher than its DC voltage (modulation index $m_k^* \le 1$). According to the analysis in [23], the stable operation range of each converter can be given as

$$V_{ac,k} = M_k V_{dc,k} = \frac{S_k V_g}{S_{total}} = \sqrt{\frac{P_k^2 + Q_k^2}{P_{total}^2 + Q_{total}^2}} V_g \le V_{dc,k} \tag{9}$$

where $V_{ac,k}$, V_g and M_k are the amplitudes of $v_{ac,k}$, v_g and m_k^*, respectively, $V_{dc,k}$ and S_k are the DC voltage and the apparent power for the k^{th} converter, respectively, and S_{total} is the apparent power for the entire system. When there is no reactive power, the criterion to determine the operation region of the k^{th} converter can be simplified as

$$\left|\frac{P_k}{P_{total}}\right| \le \frac{V_{dc,k}}{V_g}. \tag{10}$$

For the battery converter, $V_{dc,k}$ can be considered fixed in the analysis, since it does not change significantly with the variation of the battery SoC. For PV converters, their DC voltages are related to the PV power, which can be expressed as (in the standard test condition (STC)) [45]

$$P_k = V_{PV,k} I_{PV,k} = V_{PV,k}\left[I_{sc} - I_0\left(e^{\frac{V_{PV,k} + I_{PV,k}R_s}{V_t}} - 1\right)\right]. \tag{11}$$

where I_{sc} is the PV short circuit current in STC, and I_0, V_t and R_s are constants which can be obtained referring to [45]. Since PV voltages are always equal or higher than the MPP voltage in series systems due to the AOM control [33], [38], for any P_k, a specific $V_{PV,k}$ can be found. Thus, $V_{PV,k}$ can be considered as a function of P_k, and the operation region of PV converters can be rewritten as

$$\left|\frac{P_k}{P_{total}}\right| \le \frac{f(P_k)}{V_g}. \tag{12}$$

With the above, the operation boundary of a 3-cell series-PV-battery system with two PV converters and one battery converter can be illustrated in Fig. 15, and the parameters of the system are given in Table I. PV converters are considered operating in the STC in the analysis ($P_{PV1,avai} = P_{PV2,avai} = 1$ kW).

As it can be observed from Fig. 15, the operation boundary of the system is dependent on the power of individual

TABLE I
PARAMETERS OF THE SYSTEM FOR THE OPERATION BOUNDARY ANALYSIS.

PV parameters per panel at the STC	Value
Open circuit voltage V_{oc}	333.7 V
Short circuit current I_{sc}	4.33 A
MPP voltage V_{MPP}	261.5 V
MPP current I_{MPP}	3.824 A
Maximum power P_{MPP}	1000 W
Parameters for the battery converter	
Nominal voltage	144 V
Maximum charging/discharging power	±600 W
Grid parameter	
Grid nominal voltage v_g (RMS)	230 V

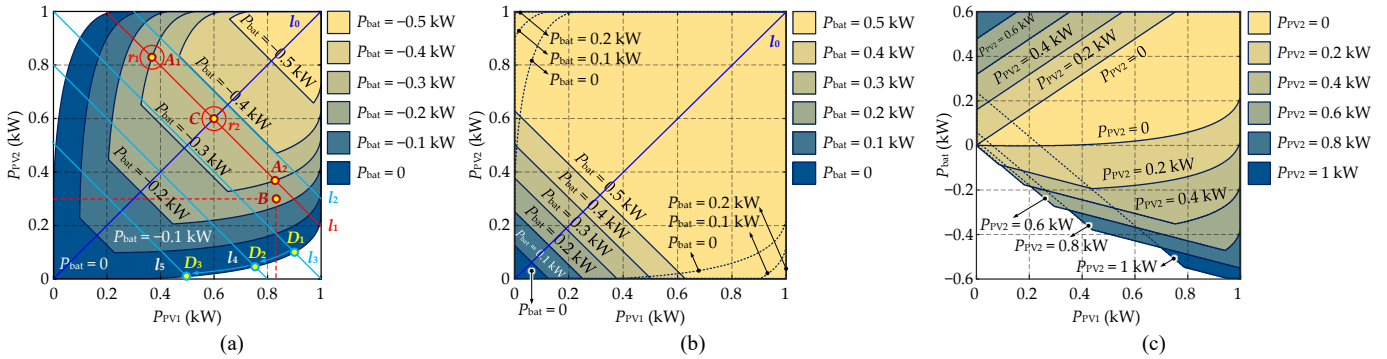

Fig. 15. Operation boundaries of a 3-cell series-PV-battery system with two PV converters and one battery converter: (a) boundaries with $P_{bat} \le 0$, (b) boundaries with $P_{bat} \ge 0$, and (c) boundaries with P_{PV2} varying from 0 to 1 kW.

converters. When P_{bat} is positive, the operation region of the system is much larger than that when P_{bat} is negative. If more power is absorbed by the battery, the operation region for the system will be narrower, as shown in Fig. 15(a). On the other hand, when P_{bat} is positive, the boundary is broadened along the diagonal from the upper left to lower right on Fig. 15(b), while the boundary at the lower left corner is narrowed. It means that when the battery is generating larger active power, the two PV converters can be more unbalanced; meanwhile, the two PV converters should also provide sufficient power to ensure the stable operation of the system (e.g., the total PV power should be at least 625 W when P_{bat} = 500 W, as shown in Fig. 15(b)).

In the proposed FAPC strategies, if the battery cannot absorb all excessive power, the power from each PV converter will be curtailed to almost the same level. With such a power curtailment, the operation points of the PV converters are maintained near the diagonal being $P_{PV1} = P_{PV2}$ (l_0) on Figs. 15(a) and (b). On the other hand, if the curtailed power is not properly distributed, the system may operate beyond the allowed boundary. For instance, as shown in Fig. 15(a), when $P^*_{total,lim}$ = 900 W and P_{bat} is limited to −300 W (P_{total} = 1.2 kW), (P_{PV1}, P_{PV2}) can be any point between A_1 (371 W, 829 W) and A_2 (829 W, 371 W) on line l_1. However, if P_{PV2} is further curtailed to 300 W, PV converter #1 will be over-modulated if it generates the desired 900 W. Due to the AOM control, P_{PV1} will be curtailed to keep the stable operation of the system, and the battery charging power will be decreased as well to keep P_{total} = 900 W. In steady state, as shown in Fig. 15(a), the system will be operated at point B, where P_{PV1} is curtailed to 830 W, while the battery is charged at -230 W. It can be noticed that 70-W power is lost because of the unbalanced curtailed power distribution. Considering that the operation points may vary due to the perturbation of the modified MPPT (e.g., within a circular range around the desired point, such as the r_1 and r_2 around A_1 and C in Fig. 15(a), respectively), the operation point C on l_0 can be more appropriate than A_1, which has larger margin with respect to the boundary. Thus, the proposed curtailed power distribution strategy, the system can operate within the allowed operation boundary with the largest margin, ensuring a good utilization of the PV power.

The equalized power loading among all PV converters can ensure the stable operation of the system with the PRRC and PLC. However, for the PRC, the system is more easily to become unstable, especially when the required power reserve is high. This is because the operation point of the system can be closer to the boundary when observing the MPPs of PV converters. For instance, if $P^*_{total,res}$ = 700 W and P_{bat} = 0, the system can be stably operated, as shown in Fig. 15(a), where the operation points of the system move along the line l_2, which is located within the operation boundary. Whereas, if $P^*_{total,res}$ is increased to 1 kW, the system will become unstable. Initially, the operation point of the system will vary along the line l_3 as shown in Fig. 15(a). However, when observing the MPPs of PV converters, the point where (P_{PV1}, P_{PV2}) = (1 kW, 0) cannot be reached because of the potential over-modulation. Consequently, the operation point of the system can only reach D_1, where $P_{PV1,avai}$ is estimated as 900 W. Similarly, $P_{PV2,avai}$ is estimated as 900 W as well. Then, the total power reference P^*_{total} will be decreased to 0.8 kW ($P^*_{total,avai}$ decreases to 1.8 kW), and the operation point of the system will vary along the new line l_4. However, as the points where P_{PV1} = 1 kW and P_{PV2} = 1 kW are still not reachable, the movement of the operation point will be stopped at D_2 when estimating $P_{PV1,avai}$, with the observed $P_{PV1,avai}$ even smaller than the value on D_1. In this way, the observed total available power will keep decreasing along the operation boundary, until it reaches C_3, where the estimated $P_{PV1,avai} = P_{PV2,avai}$ = 0.5 kW, and the system will stop operating because P^*_{total} is decreased to 0. The power reserve control will become unstable in such condition.

The above-mentioned issue can be addressed by broadening the operation boundary of the system. One possible way is to utilize low-order harmonics, which can increase the limitation of M_k higher than 1, e.g., being 1.15 as in [23]. On the other hand, the operation region of the system can also be extended by injecting reactive power to the grid [19] or increasing the battery voltage. Both approaches will loosen the criterion in (9). However, those are not the focus of this paper.

V. Experimental Validation

To validate the effectiveness of the proposed control, experiments have been performed on a 3-cell series-PV-battery system, as shown in Fig. 16, which is assembled with three Infineon FS50R12KT4_B15 IGBT modules. Two programmable DC power supplies were used to emulate the two PV

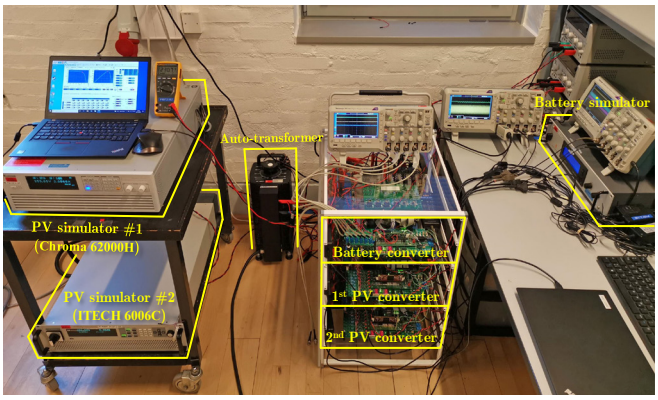

Fig. 16. Experimental prototype of the 3-cell series PVBH systems.

modules, and one DC power supply in parallel with a resistor bank was adopted to mimic the battery. Three TMS320F28335 digital signal processors were employed as individual controllers, which are interlinked with the RS-485 serial communication using the Modbus protocol. The key parameters of the series-PV-battery system are shown in Tables I and II, unless otherwise noted. In addition, as the three operational modes for the PRRC, PLC and PRC are similar in term of the surplus power distribution, the operational modes where the surplus power is partially discarded (Modes 2 for the proposed PRRC, PLC and PRC) are only validated with experimental results for the PRC. In addition, according to (8), $T_{P2,min} = 2.4$ s, $T_{P1,min} = 1$ s (only considering the cut-off frequency of the 1-Hz rectangular window LPF), and the minimum T_{MPO} can be obtained as 6.8 s. However, considering the analysis Section III. D, T_{P1}, T_{P2} are increased to ensure a more reliable MPP estimation and better control performance in terms of the power reserve distribution.

Case 1: The ramp-up and the power limiting control performance are shown in Figs. 17−19, where PV #1 and #2 are operating at 55% and 100% of their rated power in the initial stage, respectively. Then, the power of PV #1 jumps to 100% of its rated power. As shown in Fig. 17, P_{PV1} quickly increases from 506 W to 920 W, while P_{total} increases slowly following a ramp-rate of 40 W/s, with the excessive power compensated by the battery converter. In steady state, P_{total} is limited to 1600 W, and the surplus power of 240 W is absorbed by the battery. From Fig. 18, it can be noticed that the DC voltages for both PV converters are oscillating in a three-stair manner, indicating that they are operating at their MPPs during the entire process. Before and after the power step change, the line current is kept in phase with the grid voltage, as well as the AC output voltages of PV converters, as shown in the zoomed-in plots in Figs. 18 and 19. This indicates unity power factor operation of the PV converters, as well as the series system.

Case 2: To demonstrate the control performance of the system under the PLC with different battery SoC conditions, experimental results are shown in Figs. 20 and 21. The initial condition is the same with the steady-state condition of Case 1, and the *Charging_DSABL* control signal is subsequently enabled. As a result, the power of the battery converter gradually rises and oscillates around zero, which means that the battery converter is neither in the charging nor in the discharging mode. To keep the total power under the required 1600-W power limit, 120-W active power is curtailed from each PV converter, and P_{PV1} and P_{PV2} are oscillating around 800 W in steady state, as it can be observed from Fig. 20. The power curtailment of PV converters can be confirmed by the PV voltages shown in Fig. 21, where the PV voltages are oscillating around 285 V in steady state, which is higher than their MPP voltage. During the entire process, the total power and the grid current are stable, with the amplitude of the grid current being around 9.8 A, as shown in Fig. 21.

Case 3: The ramp-down control performance is demonstrated in Figs. 22−24, where the initial condition is the same with the steady-state condition of Case 2. Then, the power of PV #1 suddenly decreases to 60% of its rated power, as shown in Fig. 22, where P_{PV1} decreases abruptly and oscillates around 550 W, while PV #2 keeps operating at its full power. According to the results in Figs. 22 and 23(a), the envelope of the grid

TABLE II
HARDWARE AND CONTROL PARAMETERS FOR THE EXPERIMENTAL SETUP.

Circuit parameters	Value
DC link capacitor for PV converters	1360 μF
DC link capacitor for the battery converter	680 μF
Output LC filter of each converter	1.8 mH / 30 μF
Grid nominal voltage v_g (RMS)	230 V
Grid nominal frequency	50 Hz
Battery capacity	20 Ah
Control parameters for power loops	**Value**
Switching frequency	10 kHz
Controller sampling frequency	10 kHz
MPPT sampling rate	5 Hz
MPPT step-size	6 V
Power control parameters for PV converters[a]	$k_{p,p} = -2$, $k_{i,p} = -2$, $k_{p,q} = 0.12$, $k_{i,q} = 0.4$
Power control parameters for the battery converter[b]	$k_{p,p,total} = k_{p,q,total} = 0.005$, $k_{i,p,total} = k_{i,q,total} = 1$
Threshold for AOM loops [33]	$m_{th,L} = 0.85$, $m_{th,H} = 0.9$
Communication baud rate	9600 b/s
Flexible power control parameters	**Value**
Total power limit	$P_{total,lim} = 1600$ W
Power limits for the battery converter	$P_{bat,uplim} = 450$ W, $P_{bat,lwlim} = -450$ W
Thresholds for the battery power control	$P_{th,nrrw} = 10$ W, $P_{th,wide} = 20$ W
Comparison threshold for the PLC of PV converters	$P_{PV,th} = 50$ W
Perturbation step-size of the PLC	$V_{step,PLC} = 2$ V
Control periods for the PRC	$T_{P1} = 3$ s, $T_{P2} = 7$ s, $T_{MPO} = 20$ s
Fraction value when enabling the MPPT	$F_v = 0.783$
Low-pass filter to calculate the average power for PRC	1-Hz rectangular window, $f_{s,LPF} = 200$ Hz[d]

[a] $k_{p,p}$, $k_{i,p}$, $k_{p,q}$, and $k_{i,q}$ are the proportional and integral gains for the active and reactive power control, correspondingly.
[b] $k_{p,p,total}$, $k_{i,p,total}$, $k_{p,q,total}$ and $k_{i,q,total}$ are the proportional and integral gains for the active and reactive power control loops in the battery converter, correspondingly.
[d] $f_{s,LPF}$ is the sampling frequency for the low-pass filter.

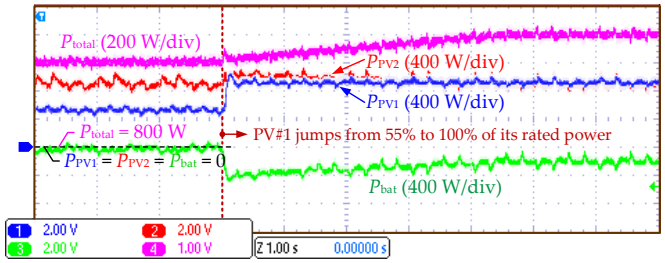

Fig. 17. Power ramp-up and power limiting control performance when PV power increases and battery charging is permitted (time [1 s/div]).

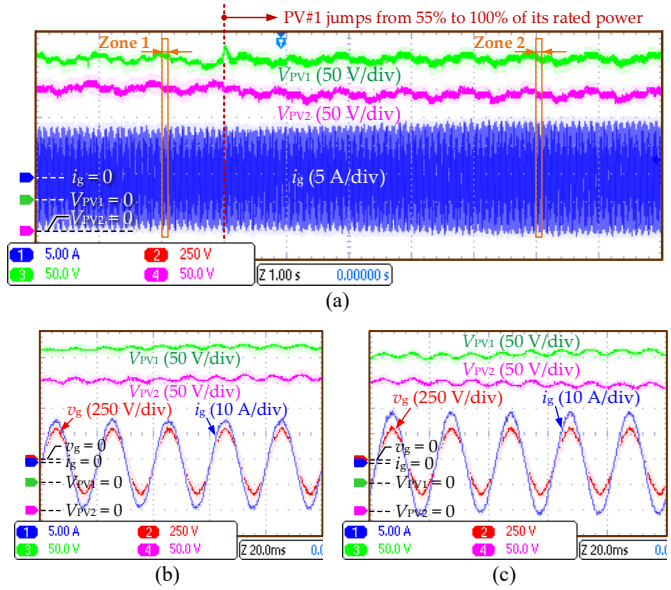

Fig. 18. Current and voltage responses of the system under power ramp-up control and PLC while the battery charging is permitted (the time scale is 1 s/div for Fig. 18(a), and 20 ms/div for Figs. 18(b) and (c)): (a) PV voltages, grid voltage and current, (b) zoomed-in plot of Zone 1 in Fig. 18(a), and (c) zoomed-in plot of Zone 2 in Fig. 18(a).

current slowly decreases, as well as the total active power, which is decreases with a ramp-rate of −40 W/s after the power step change. During the ramp-down period, the transient power is provided by the battery, with the peak power being 360-W. In steady state, both PV converters are back to their MPPs, as shown in Fig. 23(a), and P_{bat} oscillates around zero again. Before and after the step change, the line current and the ac voltages of the two PV converters are in-phase with the grid voltage, as it can be observed from Figs. 23(b), 23(c), 24(b) and 24(c), indicating that there is no reactive power contribution from the entire system and the two PV converters.

Case 4: The control performance of the PRC is demonstrated in Figs. 25 and 26. In the following cases, $v_{step,PLC}$ is set as 6 V, and the power control thresholds $P_{th,nrrw}$ and $P_{th,wide}$ are re-assigned as 20 W and 30 W, respectively. At the beginning, $P^*_{total,res}$ is set as zero, and the lower power limit of the battery converter $P_{bat,lwlim}$ is set as −200 W. The 1st and the 2nd PV converter provide approximately 700-W and 680-W active power, respectively. Due to the power control dead-band induced by the threshold P_{th}, the battery converter also provides a small part of power, which is around 20 W. The total power is thus around 1400 W, being 20-W higher than the total

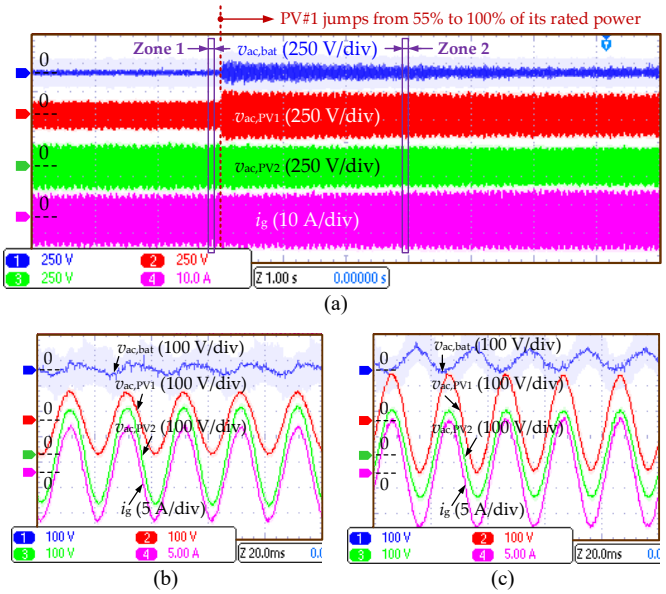

Fig. 19. Voltage responses of individual converters under power ramp-up control and PLC while the battery charging is permitted (the time scale is 1 s/div for Fig. 19(a), and 20 ms/div for Figs. 19(b) and (c)): (a) ac output voltages of individual converters and the grid current, (b) zoomed-in plot of Zone 1 in Fig. 19(a), and (c) zoomed-in plot of Zone 2 in Fig. 19(a).

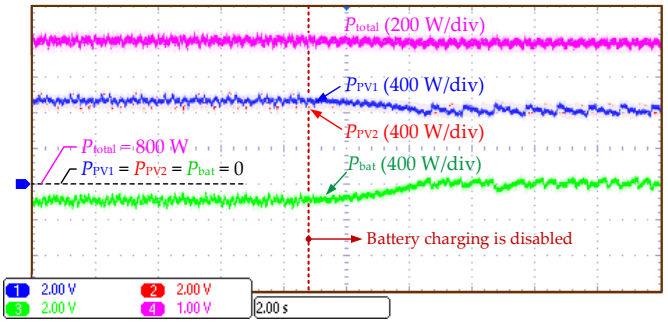

Fig. 20. Power limiting control performance when the battery charging is disabled (time [2 s/div]).

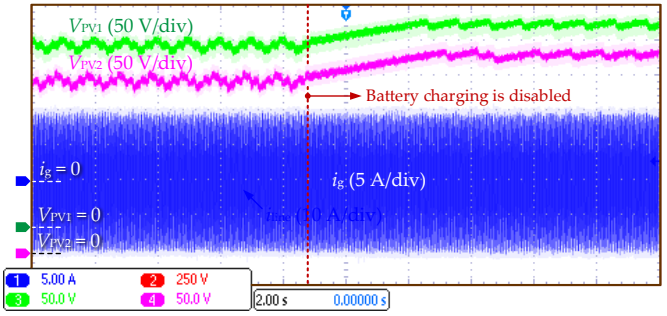

Fig. 21. Current and voltage responses of the system under PLC when the battery charging is disabled (time [2 s/div]).

available 1380-W power, as it can be observed from Fig. 25. The two PV voltages are oscillating around 260 V, which implies that the two PV converters are operating at their MPPs, as shown in Fig. 26(a). Then, in Stage II, the required power reserve is increased to 100 W. As a result, the average total power gradually decreases to 1300 W with a ramp-rate of −5.5 W/s, while all reserved power is absorbed by the battery converter. The two PV converters keep operating at their MPPs,

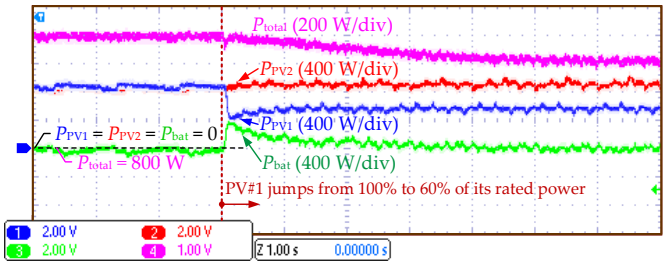

Fig. 22. Power ramp-down control performance when PV power decreases (time [1 s/div]).

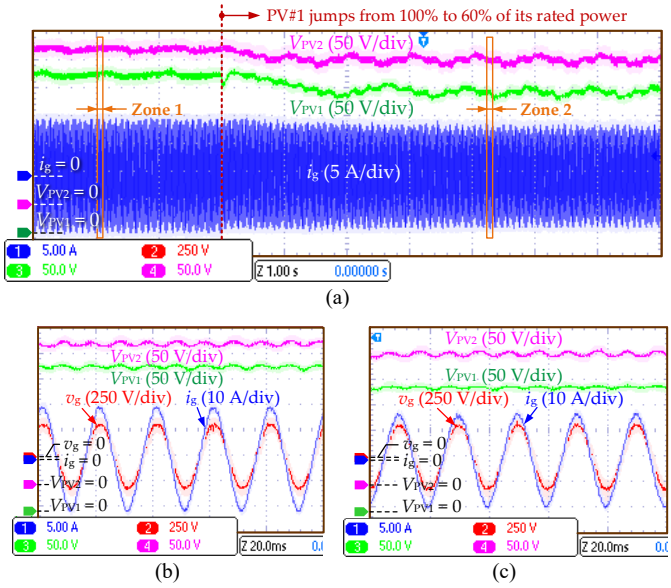

Fig. 23. Current and voltage responses of the system during power ramp-down (the time scale is 1 s/div for Fig. 23(a), and 20 ms/div for Figs. 23(b) and (c)): (a) PV voltages and the grid current, (b) zoomed-in plot of Zone 1 in Fig. 23(a), and (c) zoomed-in plot of Zone 2 in Fig. 23(a).

which can be confirmed by Figs. 25 and 26(a), where $P_{PV1,avg}$ and $P_{PV2,avg}$ are around 700 W and 680 W, respectively, while the two PV voltages are oscillating around 260 V.

In the 3rd stage, $P^*_{total,res}$ is further increased to 300 W. Consequently, the average total power gradually decreases with a ramp-rate of −5.5 W/s, until it reaches 1080 W. It can be noticed that the required 300-W power reserve is accurately achieved ($P^*_{total,avai}$ = 1380 W). Since the battery power limit $P_{bat,lwlim}$ is set as −200 W, only approximately 200-W reserved power is absorbed by the battery converter, while the power of each PV converter is curtailed to be around 640 W (60-W and 40-W power curtailed from the 1st and 2nd PV converters, respectively). It can be noticed from Fig. 25 that the power of each PV converter routinely reaches its maximum power, then is curtailed to be around 640 W, and further curtailed when the other converter is operating at its maximum power. The switch between different operational modes can also be confirmed by Fig. 26(b), where it can be observed that the two PV voltages are periodically at the MPP voltage, then increased to be around 280 V due to the PRC, and further increased to 300 V to fulfil the power reserve constraint.

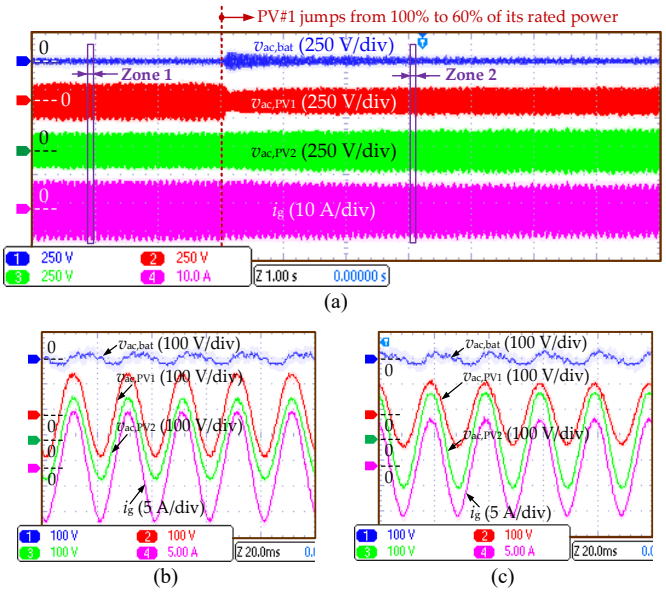

Fig. 24. Voltage responses of individual converters during power ramp-down (the time scale is 1 s/div for Fig. 24(a), and 20 ms/div for Figs. 24(b) and (c)): (a) ac output voltages of individual converters and the grid current, (b) zoomed-in plot of Zone 1 in Fig. 24(a), and (c) zoomed-in plot of Zone 2 in Fig. 24(a).

In Stage IV, due to a high SoC, the battery charging is disabled by setting $P_{bat,lwlim}$ as 0. As a result, the power of the battery converter quickly rises and oscillates around zero, while more power is curtailed from PV converters to fulfil the 300-W power reserve requirement. As shown in Fig. 25, both two PV converters periodically operate in the MPPT mode, with the observed maximum power being 700 W and 680 W for the 1st and 2nd PV converters, respectively. Thus, the power-limiting threshold $P^*_{PV,PLC}$ can be calculated as 540 W according to (5). It is in accordance with the results of Stage IV in Fig. 25, where it can be observed that when neither PV converters are operating in the MPPT mode, the power of each converter is curtailed to be around 540 W. Also, in the power-limiting periods (Periods II for both PV converters) of Stage IV, the PV voltages are increased to be around 295 V, as shown in Fig. 26(a), which confirms that more power is discarded from the two PV converters. The switch between different operational modes for PV converters can also be confirmed in Fig. 26(b), where the oscillation on the amplitudes of $v_{ac,PV1}$ and $v_{ac,PV2}$ become more obvious in Stage IV, being in a three-stair manner.

Case 5: Finally, the control performance of the PRC with different irradiance for PV panels is shown in Figs. 27 and 28, where a 300-W power reserve is required while the battery charging is disabled ($P_{bat,lwlim}$ = 0), and the initial condition is the same with the steady-state condition of Case 4. Then, in Stage II, the maximum power of the 1st PV converter is increased by 80 W. As it can be observed from Fig. 27, after the power step up, the estimated available power for the 1st PV converter is increased to 780 W, while $P_{PV2,avai}$ remains unchanged at 680 W. The total power can be accordingly calculated as 1460 W, and the total power is thus curtailed to 1160 W, as shown in Fig. 27. The two PV converters routinely

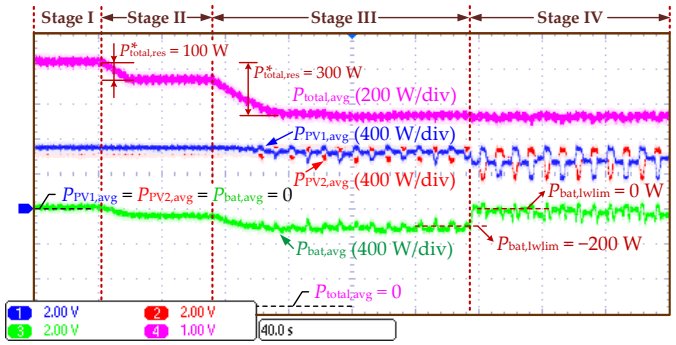

Fig. 25. Power control performance of the proposed PRC with different power reserve requirement and battery SoC conditions (time [40 s/div]).

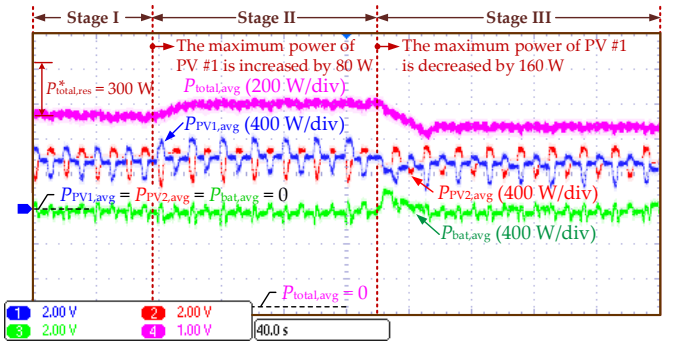

Fig. 27. Power control performance of the proposed PRC with varying irradiance for the 1st PV converter (time [40 s/div]).

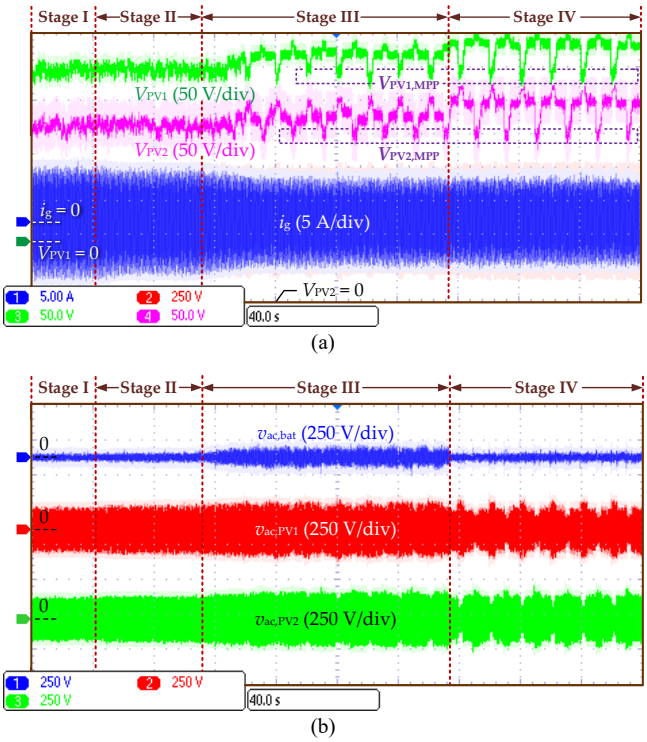

Fig. 26. Voltage and current response of the system in Case 4 of the experimental tests (time [40 s/div]): (a) PV voltages and the grid current, and (b) output ac voltages of individual converters.

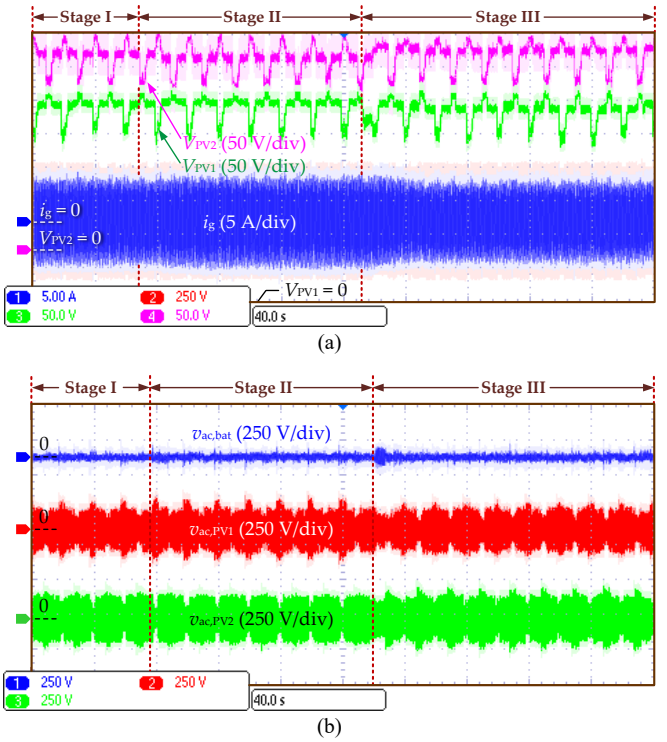

Fig. 28. Voltage and current response of the system in Case 5 of the experimental tests (time [40 s/div]): (a) PV voltages and the grid current, and (b) output ac voltages of individual converters.

operate in the MPPT mode and the power-limiting mode, which can be confirmed by the PV voltages in Fig. 28, with most reserved power being curtailed from the 1st PV converter. In the power limiting period (Period II), the power of each PV converter is limited to be around 590 W, being slightly higher than the desired $P^*_{PV,PLC}$, which can be calculated as 580 W according to (5). These small errors in the power control may possibly due to the low bandwidths of the low-pass filters (LPFs) to calculate the average power. As shown in Table II, the bandwidths of the LPFs are lower than 1 Hz, being much lower than the bandwidth of the MPPT control, which will lead to slow dynamic response of the PV power control. However, these errors have negligible influence on the PRC performance of the system, as the excessive 20-W power can be compensated by the battery to maintain the PRC constraint, as shown in Fig. 27, where $P_{bat,avg}$ is around −20 W.

In the next stage, the maximum power of the 1st PV converter is then decreased by 160 W, while it remains constant for the 2nd PV converter (680 W). As shown in Fig. 27, after the power step down, the total average power of the system gradually decreases with a ramp-rate of −5.5 W/s, until it reaches the steady-state 1020 W. Compared with the desired 1000-W total power, it can be noticed that 20-W more power is generated due to the control dead-band of P_{th}, In steady state, the periodical MPPT operation has correctly estimated the available power of PV converters, being about 620 W and 680 W for the 1st and 2nd PV converters, respectively. In the power limiting periods for both PV converters, the power of each PV converters is curtailed to be around 520 W, while almost no power is absorbed by the battery converter, which brings no change to the battery SoC.

From the above experimental results, it can be noticed that the power of the battery converter is not strictly controlled within the desired power range, e.g., being always larger than $P_{bat,lwlim}$, which is mainly due to the low bandwidth of the proposed PRC. As the battery converter is also responsible for compensating the power variation from other converters while maintaining the PRC constraints, the instantaneous power of the battery converter can easily be beyond the desired range, as shown in Figs. 25 and 27. Thus, larger margins should be considered when designing the battery converter, especially for the maximum allowed charging power. In addition, due to the low bandwidth of the LPFs employed to measure the average power, the PV power may not be precisely curtailed to the desired level, as it can be observed from Stage IV of Fig. 27, Stages II, and III of Fig. 27. Nevertheless, the PRC of the entire system is not affected by these errors in the PV power control, as they can actually be compensated by the battery converter. Since the errors are relatively small, it also has little impact on the variation of the battery SoC. Moreover, there are also a small error in the total power control due to the control dead-band being $[-P_{th}, P_{th}]$, as discussed previously. As it is very small (less than 1.25% of the rated power for the entire system), this is also acceptable in practice.

Nevertheless, the power control errors due to the control dead band can still charge/discharge the battery cumulatively, which appears in Case 5, where P_{bat} is not precisely at zero in steady state. To address this, a simple SoC balancing loop can be considered, where two thresholds SoC_{up+} and SoC_{up-} ($SoC_{up+} > SoC_{up-}$) are assigned to the SoC upper limit (SoC_{up}). More specifically, when the battery SoC reaches SoC_{up-}, $P^*_{bat,BMS}$ and $P_{bat,lwlim}$ can be set as zero. If the cumulative charge appears, $P^*_{bat,BMS}$ and $P_{bat,lwlim}$ will be set as positive values once the battery SoC reaches SoC_{up+}, which will discharge the battery. When the battery SoC is reduced back to SoC_{up-}, $P^*_{bat,BMS}$ and $P_{bat,lwlim}$ are set as zero again. Through this hysteresis control, the cumulative charging due to the power control dead-band can be avoided. Similarly, two thresholds SoC_{dw+} and SoC_{dw-} ($SoC_{dw+} > SoC_{dw-}$) can be assigned to the SoC lower limit (SoC_{dw}) to address the potential cumulative discharging of the battery.

VI. Conclusions

To achieve flexible active power control of grid-connected series-PV-battery systems, PRRC, PLC, and PRC strategies were developed in this paper. With the proposed strategies, the total PV power can be controlled following the power ramp-rate/limiting/reserve constraint commands, while all converters are coordinately controlled considering various constraints, including the total power constraints, battery power and SoC limits, and the available power of individual PV converters. The reserved/curtailed power is distributed among all converters to 1) balance the loading among all PV converters and 2) avoid the overcharging and overloading of the battery converter, ensuring a good harvesting of PV power. In the proposed PRC strategy, the MPP observation of individual PV converters is achieved by the coordinated control of all converters, which maintains the total power reserve constraints simultaneously. With this coordinated MPPT, the operation of the PRC is divided into three operation stages, where individual PV converters are in the MPPT mode, the power-limiting mode, and coordinated controlled to assist the MPP observation of other converters, respectively. In addition, the proposed control can be realized with very low communication requirements, being suitable for distributed systems. Experimental results from the hardware prototype have validated the effectiveness of the proposed control solution in terms of the PRRC, PLC, and PRC strategies, where experimental tests with the power ramp-rates being ± 2.5% and ± 0.34% of the rated power per second, total power limit being 87% of the maximum PV power, and power reserve being around 22% of the total power were performed.

References

[1] Y. Yang, K. A. Kim, F. Blaabjerg, and A. Sangwongwanich, *Advances in Grid-Connected Photovoltaic Power Conversion Systems*, Publisher: Woodhead Publishing, 2018.

[2] Energinet.dk, "Technical regulation 3.2.2 for PV power plants with a power output above 11 kW," Tech. Rep. Doc. 14/17997-39, 2015.

[3] H. D. Tafti, A. Sangwongwanich, Y. Yang, J. Pou, G. Konstantinou, and F. Blaabjerg, "An adaptive control scheme for flexible power point tracking in photovoltaic systems," *IEEE Trans. Power Electron*., vol. 34, no. 6, pp. 5451-5463, Jun. 2019.

[4] Z. Li, Z. Cheng, J. Si, S. Zhang, L. Dong, S. Li, and Y. Gao, "Adaptive power point tracking control of PV system for primary frequency regulation of ac microgrid with high PV integration," *IEEE Trans. Power Syst*., vol. 36, no. 4, pp. 3129-3141, Jul. 2021.

[5] A. Sangwongwanich, Y. Yang, and F. Blaabjerg, "A sensorless power reserve control strategy for two-stage grid-connected PV systems," *IEEE Trans. Power Electron*., vol. 32, no. 11, pp. 8559-8569, Nov. 2017.

[6] European Network of Transmission System Operators for Electricity, "Network code for requirements for grid connection applicable to all generators," Tech. Rep, Apr. 2016.

[7] S. Adhikari and F. Li, "Coordinated V-f and P-Q control of solar photovoltaic generators with MPPT and battery storage in microgrids," *IEEE Trans. Smart Grid*, vol. 5, no. 3, pp. 1270-1281, May 2014.

[8] Q. Zhang and K. Sun, "A flexible power control for PV-battery hybrid system using cascaded H-bridge converters," *IEEE J. Emerg. Sel. Topi. Power Electron*., vol. 7, no. 4, pp. 2184-2195, Dec. 2019.

[9] S. Moury and J. Lam, "A soft-switched power module with integrated battery interface for photovoltaic-battery power architecture," *IEEE J. Emerg. Sel. Topi. Power Electron*., vol. 8, no. 3, pp. 3090-3110, Sept. 2020.

[10] J. Nie, L. Yuan, W. Wen, R. Duan, B. Shi, and Z. Zhao, "Communication-independent power balance control for solid state transformer interfaced multiple power conversion systems," *IEEE Trans. Power Electron*., vol. 35, no. 4, pp. 4256-4271, Apr. 2020.

[11] X. Zhang, T. Zhao, W. Mao, D. Tan, and L. Chang, "Multilevel inverters for grid-connected photovoltaic applications: examining emerging trends," *IEEE Power Electron. Mag.*, vol. 5, no. 4, pp. 32-41, Dec. 2018.

[12] W. Liang, Y. Liu, and J. Peng, "A day and night operational quasi-Z source multilevel grid-tied PV power system to achieve active and reactive power control," *IEEE Trans. Power Electron*., vol. 36, no. 1, pp. 474-492, Jan. 2021.

[13] H. Wu, L. Zhu, F. Yang, T. Mu, and H. Ge, "Dual-DC-port asymmetrical multilevel inverters with reduced conversion stages and enhanced conversion efficiency," *IEEE Trans. Ind. Electron*., vol. 64, no. 3, pp. 2081-2091, Mar. 2017.

[14] J. Zeng, T. Kim, and V. Winstead, "A soft-switched four-port DC-DC converter for renewable energy integration," in *Proc. IEEE ECCE*, Sep. 2018, pp. 5851–5856.

[15] Y. Lu, Z. Liu, J. Kong, D. Tang, J. Yu, and J. Ji, "A fundamental voltage and harmonics elimination control strategy for single-phase cascaded off-grid photovoltaic-storage system using hybrid modulation," in *Proc. IEEE ECCE*, Oct. 2020, pp. 321-327.

[16] A. Marquez, J. I. Leon, S. Vazquez, L. G. Franquelo, and S. Kouro, "Operation of an hybrid PV-battery system with improved harmonic performance," in *Proc. 43rd Annu. Conf. IEEE Ind. Electron. Soc*., 2017, pp. 4272–4277.
[17] N. Kim and B. Parkhideh, "Control and operating range analysis of an AC-stacked PV inverter architecture integrated with a battery," *IEEE Trans. Power Electron*., vol. 33, no. 12, pp. 10032-10037, Dec. 2018.
[18] H. Liao, X. Zhang, and X. Hou, "A decentralized control of series-connected PV-ES inverters with MPPT and virtual inertia functionality," in *Proc. IEEE APEC*, Mar. 2020, pp. 3221-3224.
[19] L. Liu, H. Li, Z. Wu, and Y. Zhou, "A cascaded photovoltaic system integrating segmented energy storages with self-regulating power allocation control and wide range reactive power compensation," *IEEE Trans. Power Electron*., vol. 26, no. 12, pp. 3545-3559, Dec. 2011.
[20] S. Bazyar, H. Iman-Eini, and Y. Neyshabouri, "A fault-tolerant method for cascaded H-bridge based photovoltaic inverters with improved active and reactive power injection capability in post-fault condition," *IEEE Trans. Ind. Electron*., DOI: 10.1109/TIE.2021.3111577.
[21] X. Guo and X. Jia, "Hardware-based cascaded topology and modulation strategy with leakage current reduction for transformerless PV systems," *IEEE Trans. Ind. Electron.*, vol. 63, no. 12, pp. 7823-7832, Dec. 2016.
[22] J. Lamb and B. Mirafzal, "Grid-interactive cascaded H-bridge multilevel converter PQ plane operating region analysis," *IEEE Trans. Ind. Appl.*, vol. 53, no. 6, pp. 5744-5752, Nov.-Dec. 2017.
[23] T. Zhao, X. Zhang, W. Mao, F. Wang, J. Xu, Y. Gu, and X. Wang., "An optimized third harmonic compensation strategy for single-phase cascaded H-bridge photovoltaic inverter," *IEEE Trans. Ind. Electron*., vol. 65, no. 11, pp. 8635-8645, Nov. 2018.
[24] L. Du and J. He, "A simple autonomous phase-shifting PWM approach for series-connected multi-converter harmonic mitigation," *IEEE Trans. Power Electron.*, vol. 34, no. 12, pp. 11516-11520, Dec. 2019.
[25] J. He, Y. Li, B. Liang, and C. Wang, "Inverse power factor droop control for decentralized power sharing in series-connected-microconverters-based islanding microgrids," *IEEE Trans. Ind. Electron*., vol. 64, no. 9, pp. 7444–7454, Sep. 2017.
[26] X. Hou, Y. Sun, H. Han, Z. Liu, W. Yuan, and M. Su, "A fully decentralized control of grid-connected cascaded inverters," *IEEE Trans. Sustain. Energy*, vol. 10, no. 1, pp. 315–317, Jan. 2019.
[27] X. Hou, Y. Sun, X. Zhang, G. Zhang, J. Lu, and F. Blaabjerg, "A self-synchronized decentralized control for series-connected H-bridge rectifiers," *IEEE Trans. Power Electron*., vol. 34, no. 8, pp. 7136-7142, Aug. 2019.
[28] H. Geng, S. Li, C. Zhang, G. Yang, L. Dong, and B. N. Mobarakeh, "Hybrid communication topology and protocol for distributed-controlled cascaded H-Bridge multilevel STATCOM," *IEEE Trans. Ind. Appl*., vol. 53, no. 1, pp. 576–584, Jan./Feb.2017.
[29] H. Jafarian, S. Bhowmik, and B. Parkhideh, "Hybrid current-/voltage-mode control scheme for distributed AC-stacked PV inverter with low-bandwidth communication requirements," *IEEE Trans. Ind. Electron.*, vol. 65, no. 1, pp. 321-330, Jan. 2018.
[30] L. Li, Y. Sun, H. Han, G. Shi, M. Su, and M. Zheng, "a decentralized control for cascaded inverters in grid-connected applications," *IEEE Trans. Ind. Electron*., vol. 67, no. 9, pp. 8064-8071, Sept. 2020.
[31] P.-H. Wu, Y.-C. Su, J.-L. Shie, and P.-T. Cheng, "A distributed control technique for the multilevel cascaded converter," *IEEE Trans. Ind. Appl*., vol. 55, no. 2, pp. 1649-1657, Mar.-Apr. 2019.
[32] X. Hou, K. Sun, X. G. Zhang, Y. Sun, and J. Lu, "A hybrid voltage/current control scheme with low-communication burden for grid-connected series-type inverters in decentralised manner," *IEEE Trans. Power Electron*., vol. 37, no. 1, pp. 920-931, Jan. 2022.
[33] Y. Pan, A. Sangwongwanich, Y. Yang, and F. Blaabjerg, "Distributed control of islanded series PV-battery-hybrid systems with low communication burden," *IEEE Trans. Power Electron.*, vol. 36, no. 9, pp. 10199-10213, Sept. 2021.
[34] Y. Ko, M. Andresen, G. Buticchi, and M. Liserre, "Power routing for cascaded H-bridge converters," *IEEE Trans. Power Electron.*, vol. 32, no. 12, pp. 9435-9446, Dec. 2017.
[35] X. Li, H. Wen, Y. Zhu, L. Jiang, Y. Hu and W. Xiao, "A novel sensorless photovoltaic power reserve control with simple real-time MPP estimation," *IEEE Trans. Power Electron.*, vol. 34, no. 8, pp. 7521-7531, Aug. 2019.
[36] E. I. Batzelis, S. A. Papathanassiou and B. C. Pal, "PV system control to provide active power reserves under partial shading conditions," *IEEE Trans. Power Electron.*, vol. 33, no. 11, pp. 9163-9175, Nov. 2018.
[37] H. D. Tafti, G. Konstantinou, J. E. Fletcher, G. G. Farivar, S. Ceballos, J. Pou, and C. D. Townsend, "Flexible power point tracking in cascaded H-bridge converter-based photovoltaic systems," in *Proc. 46th Annu. Conf. IEEE Ind. Electron. Soc.*, Oct. 2020, pp. 1826-1830.
[38] X. Zhang, Y. Hu, W. Mao, T. Zhao, M. Wang, F. Liu, and R. Cao, "A grid-supporting strategy for cascaded H-bridge PV converter using VSG algorithm with modular active power reserve," *IEEE Trans. Ind. Electron*., vol. 68, no. 1, pp. 186-197, Jan. 2021.
[39] Y. Pan, A. Sangwongwanich, Y. Yang, and F. Blaabjerg, "Flexible power control of distributed grid-connected series-photovoltaic-battery systems," in *Proc. IEEE APEC*, 2021, pp. 68-75.
[40] V. G. Monopoli, A. Marquez, J. I. Leon, M. Liserre, G. Buticchi, L. G. Franquelo, and S. Vazquez, "Applications and modulation methods for modular converters enabling unequal cell power sharing: carrier variable-angle phase-displacement modulation methods," *IEEE Ind. Electron. Mag*., DOI: 10.1109/MIE.2021.3080232.
[41] A. Marquez, J. I. Leon, V. G. Monopoli, S. Vazquez, M. Liserre, and L. G. Franquelo, "Generalized harmonic control for chb converters with unbalanced cells operation," *IEEE Trans. Ind. Electron*., vol. 67, no. 11, pp. 9039-9047, Nov. 2020.
[42] A. Marquez, V. G. Monopoli, J. I. Leon, Y. Ko, G. Buticchi, S. Vazquez, M. Liserre, and L. G. Franquelo, "Sampling-time harmonic control for cascaded H-bridge converters with thermal control," *IEEE Trans. Ind. Electron.*, vol. 67, no. 4, pp. 2776-2785, Apr. 2020.
[43] A. Marquez, V. G. Monopoli, A. Tcai, J. I. Leon, G. Buticchi, S. Vazquez, M. Liserre, and L. G. Franquelo, "Discontinuous-PWM method for multilevel N-cell cascaded H-bridge converters," *IEEE Trans. Ind. Electron*., vol. 68, no. 9, pp. 7996-8005, Sept. 2021.
[44] A. Pirooz, Y. Firouz, J. Van Mierlo, and M. Berecibar, "Voltage vector redundancy exploitation for battery balancing in three-phase CHB-based modular energy storage systems," *IEEE Trans. Ind. Electron.*, DOI: 10.1109/TIE.2021.3116562.
[45] D. Sera, R. Teodorescu, and P. Rodriguez, "Partial shadowing detection based on equivalent thermal voltage monitoring for PV module diagnostics," in *Proc. IEEE IECON*, 2009, pp. 708-713.

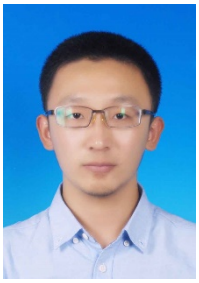

Yiwei Pan (S'19) received the B.S. degree in automation and M.S. degree in power electronics from Shandong University, Ji'nan, China, in 2015 and 2018, respectively. He is currently working toward the Ph.D. degree at Aalborg University, Aalborg, Denmark.

He was an exchange student with Tianjin University, China from July 2016 to May 2018, and a Visiting Researcher with Kiel University, Germany from August to December 2021. His current research interests include multilevel converters and distributed power generation. He was the recipient of the Best Paper Award at IEEE IPEMC-ECCE Asia 2020, and the recipient of the Best Presentation Award at IEEE APEC 2021.

Ariya Sangwongwanich (S'15-M'19) received the M.Sc. and Ph.D. degree in energy engineering from Aalborg University, Denmark, in 2015 and 2018, respectively. He is currently working as an Assistant Professor at the Department of Energy Technology, Aalborg University, where he is a Vice-Leader of Photovoltaic Systems research program. His research interests include control of grid-connected converters, photovoltaic systems, reliability in power electronics, and multi-level converters.

He was a Visiting Researcher with RWTH Aachen, Aachen, Germany from September to December 2017. Dr. Sangwongwanich was the recipient of the Danish Academy of Natural Sciences' Ph.D. Prize and the Spar Nord Foundation Research Award for his Ph.D. thesis in 2019.

Yongheng Yang (SM'17) received the B.Eng. degree in Electrical Engineering and Automation from Northwestern Polytechnical University, China, in 2009 and the Ph.D. degree in Energy Technology (power electronics and drives) from Aalborg University, Denmark, in 2014.

He was a postgraduate student with Southeast University, China, from 2009 to 2011. In 2013, he spent three months as a Visiting Scholar at Texas A&M University, USA. Since 2014, he has been with the Department of Energy Technology, Aalborg University, where he became a tenured Associate Professor in 2018. In January 2021, he joined Zhejiang University, China, where he is currently a ZJU100 Professor with the Institute of Power Electronics. His research is focused on the grid-integration of photovoltaic systems and control of power converters, in particular, the grid-forming technologies.

Dr. Yang was the Chair of the IEEE Denmark Section (2019-2020). He is an Associate Editor for several IEEE Transactions/Journals. He is a Deputy Editor of the *IET Renewable Power Generation* for Solar Photovoltaic Systems. He was the recipient of the 2018 *IET Renewable Power Generation* Premium Award and was an Outstanding Reviewer for the IEEE Transactions on Power Electronics in 2018. He received the 2021 Richard M. Bass Outstanding Young Power Electronics Engineer Award from the IEEE Power Electronics Society (PELS). In addition, he has received two IEEE Best Paper Awards. He is currently the Secretary of the IEEE PELS Technical Committee on Sustainable Energy Systems and a Council Member of the China Power Supply Society.

Xiong Liu (S'09–M'14–SM'19) received the B.E.and M.Sc. degrees in electrical engineering from Huazhong University of Science and Technology, Wuhan, China, in 2006 and 2008, respectively, and the Ph.D. degree from the School of Electrical and Electronic Engineering, Nanyang Technological University, Singapore in 2013.

From July to November 2008, he was an Engineer with Shenzhen Nanrui Technologies Company Ltd., Shenzhen, China. From September 2011 to January 2012, he was a Visiting Scholar with the Department of Energy Technology, Aalborg University, Aalborg East, Denmark. From April 2012 to December 2013, he was a Researcher with the Energy Research Institute, Nanyang Technological University. From December 2013 to July 2020, He was working as a Principal Technologist in Rolls-Royce Electrical, Rolls-Royce Singapore Pte. Ltd., Singapore. He is currently an Associate Professor with the Energy Electricity Research Center, International Energy College, Jinan University, Zhuhai, China. His research interests include power electronics, motor drive, and electrical/hybrid propulsion system for marine and aerospace.

Dr. Liu was the recipient of the Best Paper Award at the IEEE International Power Electronics and Motion Control Conference-Energy Conversion Congress and Exposition Asia in 2012.

Marco Liserre (S'00-M'02-SM'07-F'13) received the MSc and PhD degree in Electrical Engineering from the Bari Polytechnic, respectively in 1998 and 2002. He has been Associate Professor at Bari Polytechnic and from 2012 Professor in reliable power electronics at Aalborg University (Denmark). From 2013 he is Full Professor and he holds the Chair of Power Electronics at Kiel University (Germany). He has published 500 technical papers (1/3 of them in international peer-reviewed journals) and a book. These works have received more than 35000 citations. Marco Liserre is listed in ISI Thomson report "The world's most influential scientific minds" from 2014. He has been awarded with an ERC Consolidator Grant for the project "The Highly Efficient And Reliable smart Transformer (HEART), a new Heart for the Electric Distribution System". He is member of IAS, PELS, PES and IES. He has been serving all these societies in different capacities. He has received the IES 2009 Early Career Award, the IES 2011 Anthony J. Hornfeck Service Award, the 2014 Dr. Bimal Bose Energy Systems Award, the 2011 Industrial Electronics Magazine best paper award in 2011 and 2020 and the Third Prize paper award by the Industrial Power Converter Committee at ECCE 2012, 2012, 2017 IEEE PELS Sustainable Energy Systems Technical Achievement Award and the 2018 IEEE-IES Mittelmann Achievement Award.

Frede Blaabjerg (S'86–M'88–SM'97–F'03) was with ABB-Scandia, Randers, Denmark, from 1987 to 1988. From 1988 to 1992, he got the PhD degree in Electrical Engineering at Aalborg University in 1995. He became an Assistant Professor in 1992, an Associate Professor in 1996, and a Full Professor of power electronics and drives in 1998. From 2017 he became a Villum Investigator. He is honoris causa at University Politehnica Timisoara (UPT), Romania and Tallinn Technical University (TTU) in Estonia.

His current research interests include power electronics and its applications such as in wind turbines, PV systems, reliability, harmonics and adjustable speed drives. He has published more than 600 journal papers in the fields of power electronics and its applications. He is the co-author of four monographs and editor of ten books in power electronics and its applications.

He has received 33 IEEE Prize Paper Awards, the IEEE PELS Distinguished Service Award in 2009, the EPE-PEMC Council Award in 2010, the IEEE William E. Newell Power Electronics Award 2014, the Villum Kann Rasmussen Research Award 2014, the Global Energy Prize in 2019 and the 2020 IEEE Edison Medal. He was the Editor-in-Chief of the IEEE Transactions on Power Electronics from 2006 to 2012. He has been Distinguished Lecturer for the IEEE Power Electronics Society from 2005 to 2007 and for the IEEE Industry Applications Society from 2010 to 2011 as well as 2017 to 2018. In 2019-2020 he serves as a President of IEEE Power Electronics Society. He has been Vice-President of the Danish Academy of Technical Sciences.

He is nominated in 2014-2020 by Thomson Reuters to be between the most 250 cited researchers in Engineering in the world.